



P. Sharifi · M. Shojaee  · S. Salighe

Vibration of rotating porous nanocomposite eccentric semi-annular and annular plates in uniform thermal environment using TDQM

Received: 18 July 2022 / Accepted: 8 December 2022 / Published online: 30 December 2022
© The Author(s), under exclusive licence to Springer-Verlag GmbH Germany, part of Springer Nature 2022

Abstract In this paper, free vibration of rotating functionally graded (FG) porous eccentric semi-annular (ESA) and eccentric annular (EA) plates reinforced with graphene nanoplatelets (GPLs) in a thermal environment is solved with the help of transformed differential quadrature method (TDQM). Symmetrical and asymmetrical distributions are considered for both the porosity and the graphene nanoplatelets; the estimation of the Young's modulus is conducted by the model of Halpin–Tsai. A higher-order shear deformation theory is considered as the basis for the employment of the Hamilton's principle for the derivation of both the initial equations of the plates-up to the dynamic equilibrium point and the oscillation phenomena afterward. The method of TDQM utilizes a conformal mapping in order to obtain the DQ weighting coefficients and then discretizes the partial differential equations of the motion, as well as the boundary conditions; this discretization takes place in the physical domain directly. The results indicate that the employed numerical approach is advantageous in high solution accuracy in addition to fast convergence rate. Furthermore, the variation of the natural frequencies of the FG plates with different boundary conditions is investigated by taking into account the influences of several parameters: the geometry, such as eccentricity, thickness ratio, radius ratio; the material, such as the type of porosity and GPLs, the porosity parameter and the weight fraction of GPLs, and other parameters, such as temperature difference and rotating speed.

Keywords Transformed differential quadrature · Eccentric annular (EA) plate · Free vibration · Thermal environment · Porous nanocomposite

1 Introduction

During the past decades, carbon-based reinforcements, such as 1-dimensional nanotubes and 2-dimensional graphene, have been employed for enhancing the mechanical and electrical properties of composite materials. According to the development of manufacturing methods in terms of reducing the cost of raw materials, nanocomposites have been highly used in flexible batteries, manufacturing alternative bone structures in the body, structural engineering (such as aerospace, automotive and civil engineering) and lightweight sensors. Therefore, the importance of such potential and the vast application of these composite structures have raised the attention of researchers toward them. Reports of experiments demonstrate a significant increase in mechanical, thermal and physical properties of polymers, when additives such as carbon nanotubes are introduced into the polymer matrix [1, 2]. Hence, industrial societies have taken great interest in carrying out studies on the

P. Sharifi · S. Salighe
School of Mechanical Engineering, Shiraz University, Shiraz 71936-16548, Iran

M. Shojaee (✉)
Cyber-Physical Simulation Group, Department of Mechanical Engineering, Technical University of Darmstadt, Darmstadt, Germany
e-mail: shojaee@cps.tu-darmstadt.de

mechanical behavior of porous graphene-reinforced nanocomposites. Studies showed a better performance of graphene platelets in comparison with the carbon nanotube additives when it comes to mechanical properties epoxy nanocomposites; part of the results indicated that the Young's modulus of the graphene nanocomposite, at a nanofiller weight fraction of $0.1 \pm 0.002\%$, increased by 31%, whereas a rise by 3% was recorded for single-walled carbon nanotubes [2]. The stiffening effect of functionally graded graphene composite plates was compared with those reinforced with carbon nanotubes [3]. The researchers took into account the agglomeration effects as well as restacking of graphene sheets and realized a better load bearing capacity of graphene nanotubes (GNTs) compared to carbon nanotubes (CNTs).

Regarding the nonlinear behavior of composite structures, multiscale doubly curved nanocomposites nanoshells made of CNT/GPL-fiber are studied in [4]. Also, nonlinear vibration and bending characteristic of multilayered composite beams reinforced with uniform distribution and uniform dusting of graphene fibers under Timoshenko's theory were investigated by Feng et al. [5, 6]. Studying the buckling and free vibration of the same structure, Kitipornchai et al. [7] discovered that more concentration of graphene toward the outer surfaces of a composite beam rose its stiffness significantly, which led to the growth in natural frequency and the buckling load. Further studies on functionally graded graphene platelets reinforced composite (FG-GRC) structures with more complex geometries, such as toroidal panels [8] and conical shells [9], are carried out in terms of oscillatory behavior and post-buckling analysis, respectively.

A new class of lightweight materials which have internal porosity are known as metal foams. The engineering applications of such materials are restricted due to their low strength. In order to surmount this obstacle, however, carbon nanostructures are exploited which have the ability to forge a bond with the matrix, in contrast to carbon nanotubes. Consequently, the load is uniformly transferred and an increase in strength is obtained [10–13]. Materials such as these are not only able to keep the properties of porous structures [14–17] (light weight, low density and high energy absorption) but also able to gain nanocomposite characteristics (high elastic modulus, high fracture strength and high thermal conductivity). A reinforced porous nanocomposite beam constructed with functionally graded graphene was studied in terms of free vibration, nonlinear vibration, elastic buckling and post-buckling [7, 18]. The imperfection geometry was taken into account when analyzing the post-buckling of a porous beam with GPLs reinforcements mounted on a nonlinear elastic foundation [19]. The study found that the post-buckling load reached its peak when a symmetrical dispersion was considered for the porosity and the GPLs, while the minimum load was recorded for the structure with uniform porosity. In addition, better mechanical performance was obtained when the GPLs were distributed uniformly, rather than symmetrically. Similarly, investigating the impact of using GPLs on the buckling pressure of a functionally graded porous cylinder [20] showed that a non-uniform but symmetrical distribution for GPLs and porosity led to the highest pressure capacity.

For the past few years, scientists—in the fields of aeronautic, automotive industries or many others—have become more attracted to study the characteristics of the structures with round shapes [21]. Žur [22] studied the free vibration of axisymmetric and non-axisymmetric oscillation of an elastically supported FG annular plate with variety of inner boundary conditions, whereas Allahkarami [23] surveyed the impact of a periodic radial compressive load on the dynamic stability of the same structure—but reinforced with GPLs. Many articles considered the variable thickness of annular plates not only as a highly influential factor to attain economical usage of material but also as a practical mean to stiffen the structure having less weight; the thickness can change either abruptly [24] or gradually [25], along the radial direction.

One type of geometry imperfection is when the structure, especially a plate, contains one [26] or multiple [27] perforations with diverse shapes and sizes. Having these internal cutouts relocated to a further distance from the center of symmetry, one encounters even more complex mathematical formulations [28]. These eccentric cutouts can have significant effect on the vibrating behavior of EA plates [29–31]. Askari et al. [32] dealt with the partial differential equation of free and coupled-fluid vibration of these EA plates based on the separation of variables [33]. On the other hand, a systematic approach for solving FG-GRC-EA plates with integrated piezo layers is presented in [34].

Thermal environment, similar to the eccentricity, can make a noticeable difference when involved in the overall assumptions of a mechanical problem. This can be exemplified by undesired buckling or dynamic responses [35]. Since these environments with high temperatures are inevitable in many industrial procedures, structures with FG properties have become introduced by many scientists [36, 37]. Malekzadeh et al. [38] believed that the FGMs outperform those traditional composite laminates by reducing thermal stresses or stress concentrations. Recently, Lal and Saini [39] investigated the effects of thermal environments on an annular plate; in their work, in contrast to [38], the thickness of the plate is considered to be variable.

Rotating machineries are widely employed throughout industrial processes. The rotating system models can be introduced as a shaft, a shell [40] and a disk or a blade attached to the axis of rotation; in [41], the Rayleigh beam theory and Euler-Bernoulli beam theory are used to present the free vibration of a pre-twisted blade-shaft assembly; in the similar work, done by Zhao et al. [42], the natural frequencies of a disk-shaft rotor system are computed analytically and the model is built based on Kirchhoff plate theory and Timoshenko beam theory; in another model, a setting angle is considered for a pre-twisted blade, which is mounted on a rotating disk with a centric hole [43]. In another contribution [44], a plate is attached to a rotating hub modeled as an elastic cylindrical shell. For investigation of the free vibration, the dynamical model is constructed based on the Donnell shell theory and the Kirchhoff plate theory and the coupled vibration.

Another type of rotating systems is circular plate without a centric hole [45], which is among the critical components of industry, whose vibration and stability should be studied carefully [46–48]. Bagheri and Jahangiri [49] investigated the free vibration of rotating disks with FG properties. Yang and Kang [50], as well as Younesian et al. [51], published papers regarding the analysis of annular plates subjected to compressive centrifugal body force and peripheral transverse loads, respectively. The assumptions for the circular plates with off-center hole in thermal environment, in company with the rotating phenomenon, will result in enormous equations of motion. So, Transformed Differential Quadrature method (TDQM) is a powerful numerical tool for solving difficult equations of motion (especially those structures with complex shape). In this method, the discretization of the governing equations is directly conducted in the physical domain for determining the weighting coefficients [52–54].

The presented article exploits the TDQM in investigating the free vibration of a rotating FG-GRC porous semi-annular plates with an off-centered semicircle cut-out in thermal environment. To the best of the authors' knowledge acquired from the latest contributions, the TDQM has not been utilized as a numerical tool for tackling the eigenvalue problem of such ESA plates (with the proposed characteristics) yet. Two different types of porosity are considered in the analysis: the symmetrical and the asymmetrical distributions. Also, the dispersion of graphene platelets is categorized into three types: symmetrical (non-uniform), asymmetrical (non-uniform) and uniform. The Halpin–Tsai micromechanics model is proposed in order to determine the elastic modulus of graphene nanoplatelets; other mechanical properties, such as the density, Poisson's ratio and thermal expansion coefficients, are obtained using the rule of mixture.

Once the mechanical properties of the structure are defined completely, two consecutive phases are introduced, based on which the governing equations of motion are presented: the first stage—which involves in-plane deformations due to the rotation and a steady change in temperature—lasts until the dynamic equilibrium is reached; the second stage, however, is the out-of-plane oscillation phenomenon, which is then handled using a higher-order shear theory (with 7 degrees of freedom). By applying the TDQM, the obtained equations from the first and second phases are discretized directly in the physical domain using an appropriate conformal mapping. Finally, the first four natural frequencies are numerically illustrated and how variations in different parameters, such as geometry, material, boundary conditions, rotational speed and temperature would manipulate these results, are meticulously investigated for both the annular and semi-annular FG-GRC plates. Using the TDQM for tackling the governing equations of an eccentric semi-annular vibrating plate can be considered as the starting point for putting a systematic solution forward to the analysis of sector-plates with more complex structures; this, consequently, inclines the authors to put forth the presented technique for handling eccentric sector-plates in future studies.

The following section describes the geometry of the proposed structure and its mechanical properties. Then, the governing equations and the use of discretization technique in TDQM are presented. Section 3 is dedicated to the numerical results and the comprehensive parameter study. In the end, Sect. 4 summarizes the overall methodology and discusses the conclusions thoroughly.

2 Mathematical model

2.1 The geometry of the FG-GRC plates

Two eccentric plates are proposed as the mechanical structures, each of which is provided with the cylindrical coordinate system (r, θ, z) labeling the points of the structure when no deformation is occurred. These two models are defined as eccentric annular (EA) plate ($\theta = 2\pi$) and eccentric semi-annular (ESA) plate ($\theta = \pi$), having circular and semi-circular cutouts (Fig. 1), respectively. The eccentricity is denoted by \bar{e} . The thickness of the plates, the inner radius and the outer radius are h , b and a , respectively. Functionally graded distribution for porosity and graphene platelets includes diverse models along the thickness of the plates. In Fig. 2, it can

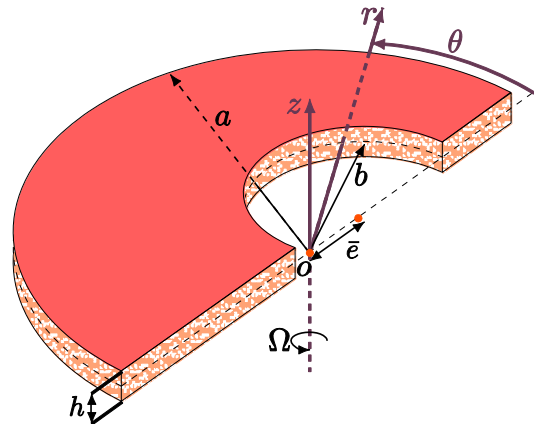


Fig. 1 The geometry of the FG-GRC-ESA plate

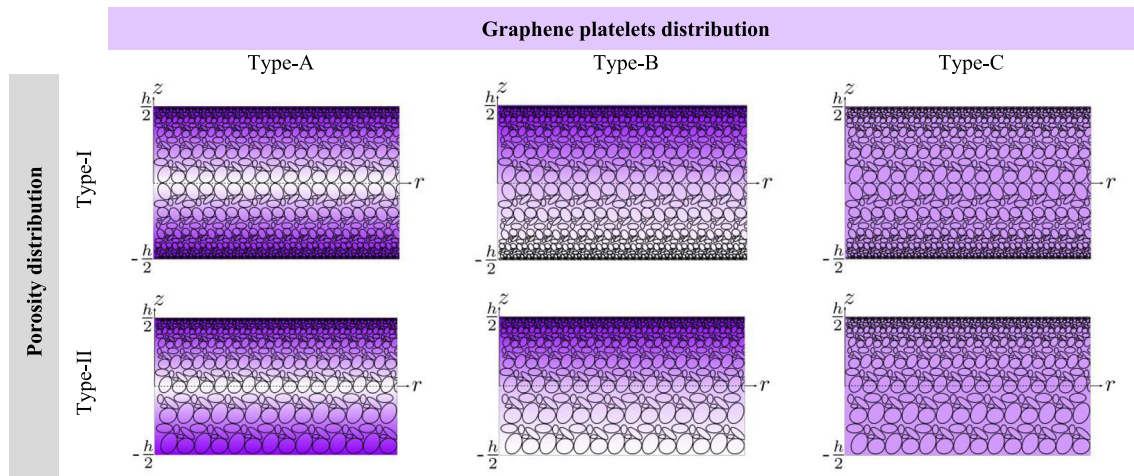


Fig. 2 Various dispersion patterns considered for the porosity and the graphene platelets

be seen that the GPLs are distributed based on three different patterns: Type-A, non-uniform and symmetrical; Type-B, non-uniform and asymmetrical; Type-C, uniform. Moreover, the pattern of porosity is categorized into two types: Type-I, symmetrical; Type-II, asymmetrical.

2.2 Material properties

The mechanical properties of the FG-GRC model with porosity, such as Young’s modulus E , shear modulus G , density ρ and thermal expansion coefficient α , are defined as functions of z [55]. We have:

$$\begin{aligned}
 E(z) &= E^*(1 - e_0\lambda(z)) \\
 G(z) &= G^*(1 - e_0\lambda(z)) \\
 \rho(z) &= \rho^*(1 - e_m\lambda(z)) \\
 \alpha(z) &= \alpha^*(1 - e_m\lambda(z)) \\
 \lambda(z) &= \begin{cases} \cos(\pi z/h) & \text{Type - I} \\ \cos(\pi z/2h + \pi/4) & \text{Type - II} \end{cases}
 \end{aligned}
 \tag{1}$$

$$\tag{2}$$

In Eq. 1, E^* , G^* , ρ^* and α^* are the corresponding mechanical properties of the nonporous FG-GRC. $\lambda(z)$ demonstrates two types of porosity distribution in the z direction, given in Eq. 2. Accordingly, Type-I is related to the symmetrical distribution, where the maximum and minimum values of porosity are at $z = 0$ and $z = \pm h/2$, respectively. In Type-II, porosity is asymmetrically distributed—the maximum/minimum value

are located at the bottom/top surface, respectively. The following relation expresses the connection between parameter e_m (mass density coefficient) and e_0 (porosity coefficient).

$$e_m = \frac{1 - \sqrt{1 - e_0 \lambda(z)}}{\lambda(z)} \tag{3}$$

In order to obtain the modulus of elasticity for the nonporous graphene-reinforced composites, Halpin–Tsai micro mechanical model [56] is employed, and hence we have:

$$E^* = \frac{3}{8} \left(\frac{1 + \xi_{GPL}^L \eta_{GPL}^L V_{GPL}}{1 - \eta_{GPL}^L V_{GPL}} \right) E_m + \frac{5}{8} \left(\frac{1 + \xi_{GPL}^W \eta_{GPL}^W V_{GPL}}{1 - \eta_{GPL}^W V_{GPL}} \right) E_m \tag{4}$$

where

$$\begin{aligned} \xi_{GPL}^L &= \frac{2l_{GPL}}{h_{GPL}}, \quad \xi_{GPL}^W = \frac{2w_{GPL}}{h_{GPL}} \\ \eta_{GPL}^L &= \frac{E_{GPL} - E_m}{E_{GPL} + \xi_{GPL}^L E_m}, \quad \eta_{GPL}^W = \frac{E_{GPL} - E_m}{E_{GPL} + \xi_{GPL}^W E_m} \end{aligned} \tag{5}$$

In Eq. 4, the polymer matrix contains E_m as the Young’s modulus. Other dimensionless parameters labeled with GPL are the properties of GPLs introduced in Eq. 5. The volume fraction in the direction of z is named V_{GPL} . In Eq. 5, E_{GPL} , l_{GPL} , w_{GPL} , and h_{GPL} are the elastic modulus, length, width, and thickness of GPLs, respectively.

Following the rule of mixture [57], one is able to express density ρ^* , Poisson’s ratio ν^* and the thermal expansion coefficient α^* of the GPLs reinforced nanocomposite without porosity, with the formulations below:

$$\begin{aligned} \rho^* &= \rho_{GPL} V_{GPL} + \rho_m V_m \\ \nu^* &= \nu_{GPL} V_{GPL} + \nu_m V_m \\ \alpha^* &= \alpha_{GPL} V_{GPL} + \alpha_m V_m \end{aligned} \tag{6}$$

where ρ_{GPL} , ν_{GPL} and α_{GPL} are density, Poisson’s ratio and the thermal expansion coefficients of GPLs, and their isotropic matrix counterparts are ρ_m , ν_m and α_m . V_m indicates the volume fraction of the matrix. The relationship of shear modulus and the elasticity modulus for the nonporous GPLs reinforced nanocomposite is obtained as follow:

$$G^* = \frac{E^*}{2(1 + \nu^*)} \tag{7}$$

Regarding the volume fraction, three different patterns (in the direction of z) are investigated [20]. Although Type-A and Type-B illustrate the symmetrical and asymmetrical distribution of graphene, they are both considered non-uniform. In the third pattern, on the other hand, the volume fraction is assumed to be uniform.

$$V_{GPL}(z) = \begin{cases} s_1(1 - \cos(\pi z/h)) & \text{Type - A} \\ s_2(1 - \cos(\pi z/2h + \pi/4)) & \text{Type - B} \\ s_3 & \text{Type - C} \end{cases} \tag{8}$$

In order to obtain the constant parameters s_i for $i = 1, 2, 3$, each pattern in Eq. 8 needs to be substituted into the following relation [58]:

$$\int_{-\frac{h}{2}}^{\frac{h}{2}} \frac{V_{GPL}}{V_{GPL}^0} (1 - e_m \lambda(z)) dz - \int_{-\frac{h}{2}}^{\frac{h}{2}} (1 - e_m \lambda(z)) dz = 0 \tag{9}$$

where

$$V_{GPL}^0 = \frac{\Lambda_{GPL} \rho_m}{\Lambda_{GPL} \rho_m + \rho_{GPL}(1 - \Lambda_{GPL})} \tag{10}$$

In Eq. 10, Λ_{GPL} is the weight fraction of GPLs.

2.3 Dynamic Equations and boundary conditions

When the free vibration of a rotating model in a thermal environment is under investigation, one is able to express the initial displacements (u_{r0} , $u_{\theta0}$, u_{z0}) as follows:

$$\begin{aligned} u_{r0} &= \bar{u}(r, \theta), \\ u_{\theta0} &= \bar{v}(r, \theta), \\ u_{z0} &= 0. \end{aligned} \quad (11)$$

where the displacement components (\bar{u} , \bar{v}) originate from both a steady change in the model's temperature (no thermal gradient is taken into account) and a dynamical rotation. These thermal and rotating characteristics only affect the in-plane displacements along the radial (r) and azimuth (θ) coordinates. Therefore, in-plane strain-displacement relations are formulated as follows [59]:

$$\begin{aligned} \varepsilon_{rr0} &= \frac{\partial \bar{u}}{\partial r}, \\ \varepsilon_{\theta\theta0} &= \frac{\bar{u}}{r} + \frac{1}{r} \frac{\partial \bar{v}}{\partial \theta}, \\ \varepsilon_{r\theta0} &= \frac{1}{r} \frac{\partial \bar{u}}{\partial \theta} - \frac{\bar{v}}{r} + \frac{\partial \bar{v}}{\partial r}. \end{aligned} \quad (12)$$

The Hamilton's principle, for the time interval t_1 to t_2 [60], suggests that:

$$\int_{t_1}^{t_2} (\delta T_0 - \delta U_0) dt = 0 \quad (13)$$

in which the kinetic energy T_0 and the potential U_0 (in their initial states) are introduced. Parameter t is time. The variations of the aforementioned energies are expressed as follows [45]:

$$\delta T_0 = \int_{\Lambda} \rho \Omega^2 [(r + \bar{u})\delta \bar{u} - \bar{v}\delta \bar{v}] d\Lambda \quad (14)$$

$$\delta U_0 = \int_{\Lambda} (\sigma_{rr0} - \sigma_{Trr0})\delta \varepsilon_{rr0} + (\sigma_{\theta\theta0} - \sigma_{T\theta\theta0})\delta \varepsilon_{\theta\theta0} + (\sigma_{r\theta0})\delta \varepsilon_{r\theta0} d\Lambda \quad (15)$$

In Eq. 14, ρ and Λ are known as the mass density and the volume of the circular plate, respectively. Additionally, the plate rotates at the speed Ω . In Eq. 15, the corresponding stresses are obtained on the basis of the former in-plane strains and Q_{ij} introduced as the elements of the reduced stiffness matrix (see Appendix A). We have:

$$\sigma_{rr0} = Q_{11}\varepsilon_{rr0} + Q_{12}\varepsilon_{\theta\theta0}, \sigma_{\theta\theta0} = Q_{12}\varepsilon_{rr0} + Q_{22}\varepsilon_{\theta\theta0}, \sigma_{r\theta0} = Q_{66}\varepsilon_{r\theta0} \quad (16)$$

On the other side, the initial thermal stresses along the radial direction and the circumferential direction are also expressed as follows:

$$\sigma_{Trr0} = (Q_{11} + Q_{12})\alpha(z)\Delta T, \sigma_{T\theta\theta0} = (Q_{12} + Q_{22})\alpha(z)\Delta T \quad (17)$$

in which ΔT shows the temperature difference between two time-intervals. It should be mentioned that the temperature is uniformly distributed throughout the whole plate in each time-interval.

By using Eqs. 14, 15, 16 and 17, as well as 12, the governing equations can be extracted from Eq. 13 as follows:

$$\begin{aligned} H_{11} \frac{\partial^2 \bar{u}}{\partial r^2} + \frac{H_{66}}{r^2} \frac{\partial^2 \bar{u}}{\partial \theta^2} + \frac{H_{11}}{r} \frac{\partial \bar{u}}{\partial r} - \frac{H_{22}\bar{u}}{r^2} - \left(\frac{H_{22}}{r^2} + \frac{H_{66}}{r^2} \right) \frac{\partial \bar{v}}{\partial \theta} + \left(\frac{H_{12}}{r} + \frac{H_{66}}{r} \right) \frac{\partial^2 \bar{v}}{\partial r \partial \theta} + \frac{N_{T\theta0}}{r} - \frac{N_{Tr0}}{r} \\ = -m_1 \Omega^2 (r + \bar{u}) \end{aligned} \quad (18)$$

$$\left(\frac{H_{22}}{r^2} + \frac{H_{66}}{r^2} \right) \frac{\partial \bar{u}}{\partial \theta} + \left(\frac{H_{12}}{r} + \frac{H_{66}}{r} \right) \frac{\partial^2 \bar{u}}{\partial r \partial \theta} + H_{66} \frac{\partial^2 \bar{v}}{\partial r^2} + \frac{H_{66}}{r} \frac{\partial \bar{v}}{\partial r} + \frac{H_{22}}{r^2} \frac{\partial^2 \bar{v}}{\partial \theta^2} - \frac{H_{66}\bar{v}}{r^2} = -m_1 \Omega^2 \bar{v} \quad (19)$$

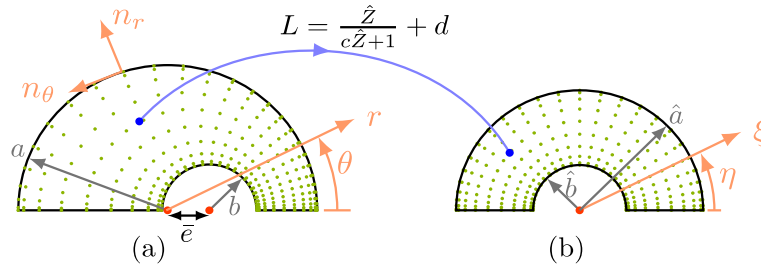


Fig. 3 The geometry of transformation for an ESA plate, **a** the physical domain, **b** computational domain

in which $H_{ij}^{\chi\kappa}$ and $m_{\chi\kappa}$ are obtained using the following relations:

$$H_{ij}^{\chi\kappa} = \int_{-\frac{h}{2}}^{\frac{h}{2}} Q_{ij} \chi(z) \kappa(z) dz$$

for $(\chi, \kappa = \{, f, g, f', g') \text{ and } (i, j = 1, 2, 4, 5, 6)$ (20)

$$m_{\chi\kappa} = \int_{-\frac{h}{2}}^{\frac{h}{2}} \rho \chi(z) \kappa(z) dz$$

for $(\chi = 1, f, g), (\kappa = \{, f, g)$ (21)

Also, for N_{Tr0} and $N_{T\theta0}$, we have:

$$\begin{bmatrix} N_{Tr0} \\ N_{T\theta0} \end{bmatrix} = \int_{-\frac{h}{2}}^{\frac{h}{2}} \begin{Bmatrix} \sigma_{Tr0} \\ \sigma_{T\theta0} \end{Bmatrix} dz$$
 (22)

Other notations of χ and κ (rather than 1) will be used in handling the free vibration of the model; also, $\chi, \kappa = \{$ means that there is no notation and the parameter is left blank.

The essential and natural boundary conditions are applied on the proposed structure (see Fig. 3). We have:

$$\text{Either } n_r \bar{u} + n_\theta \bar{v} = 0 \text{ or } n_r^2 N_{rr0} + 2n_r n_\theta N_{r\theta0} + n_\theta^2 N_{\theta\theta0} = 0$$
 (23)

$$\text{Either } -n_\theta \bar{u} + n_r \bar{v} = 0 \text{ or } n_r n_\theta (N_{\theta\theta0} - N_{rr0}) + (n_r^2 - n_\theta^2) N_{r\theta0} = 0$$
 (24)

where (n_r, n_θ) are the radial and circumferential components of the unit normal to the boundaries of the EA/ESA plate, respectively. Also, N_{rr0} , $N_{\theta\theta0}$ and $N_{r\theta0}$ are defined as

$$\begin{bmatrix} N_{rr0} \\ N_{\theta\theta0} \\ N_{r\theta0} \end{bmatrix} = \int_{-\frac{h}{2}}^{\frac{h}{2}} \begin{Bmatrix} \sigma_{rr0} + \sigma_{Tr0} \\ \sigma_{\theta\theta0} + \sigma_{T\theta0} \\ \sigma_{r\theta0} \end{Bmatrix} dz$$
 (25)

When the free vibration of the structure (with initial displacements) is to be investigated, the following formulations for the displacement field are suggested.

$$\begin{aligned} u_r &= \bar{u}(r, \theta) + \hat{u}(r, \theta, z, t), \\ u_\theta &= \bar{v}(r, \theta) + \hat{v}(r, \theta, z, t), \\ u_z &= \hat{w}(r, \theta, t). \end{aligned}$$
 (26)

in which (\bar{u}, \bar{v}) are already defined from Eqs. 18 and 19. However, according to the higher-order shear theory, $(\hat{u}, \hat{v}, \hat{w})$ can be expressed such that [61]:

$$\begin{aligned} \hat{u} &= u(r, \theta, t) + f(z)\varphi^r(r, \theta, t) + g(z)\psi^r(r, \theta, t), \\ \hat{v} &= v(r, \theta, t) + f(z)\varphi^\theta(r, \theta, t) + g(z)\psi^\theta(r, \theta, t), \\ \hat{w} &= w(r, \theta, t). \end{aligned}$$
 (27)

In Eq. 27, (u, v, w) are the displacement components in the direction of (r, θ) for the material point on the mid-surface of the EA/ESA plate where $z = 0$. $(\varphi^r, \varphi^\theta)$ are the rotations of transverse normal around

the (θ, r) . Considering the warping of the plate, two other degrees of freedom are introduced as (ψ^r, ψ^θ) . Functions (f, g) are formulated based on the third-order shear deformation theory given as follows:

$$f(z) = z - \frac{4z^3}{3h^2}, \quad g(z) = -\frac{4z^3}{3h^2} \tag{28}$$

According to the cylindrical coordinate system, the strain–displacement elements (upon which the out-of-plane oscillation phenomenon is to be investigated) with nonzero values can be expressed as [59]:

$$\begin{aligned} \varepsilon_{rr} &= \frac{\partial \hat{u}}{\partial r}, \quad \varepsilon_{rrn} = \frac{1}{2} \left(\frac{\partial \hat{w}}{\partial r} \right)^2, \quad \varepsilon_{\theta\theta} = \frac{\hat{u}}{r} + \frac{1}{r} \frac{\partial \hat{v}}{\partial \theta}, \quad \varepsilon_{\theta\theta n} = \frac{1}{2r^2} \left(\frac{\partial \hat{w}}{\partial \theta} \right)^2, \\ \gamma_{r\theta} &= \frac{1}{r} \frac{\partial \hat{u}}{\partial \theta} - \frac{\hat{v}}{r} + \frac{\partial \hat{v}}{\partial r}, \quad \gamma_{r\theta n} = \frac{1}{r} \frac{\partial \hat{w}}{\partial r} \frac{\partial \hat{w}}{\partial \theta}, \quad \gamma_{rz} = \frac{\partial \hat{u}}{\partial z} + \frac{\partial \hat{w}}{\partial r}, \quad \gamma_{\theta z} = \frac{\partial \hat{v}}{\partial z} + \frac{1}{r} \frac{\partial \hat{w}}{\partial \theta}. \end{aligned} \tag{29}$$

Notations without subscript n are connected to the linear strain components, whereas the other notations with n are the nonlinear ones.

Once again, the Hamilton’s principle is applied so that:

$$\int_{t_1}^{t_2} (\delta T - \delta U) dt = 0 \tag{30}$$

In Eq. 30, δT and δU are, respectively, the variations of kinetic and potential energy [45], written as:

$$\delta T = \int_{\Lambda} \rho \left\{ \left(\frac{\partial u_r}{\partial t} - \Omega u_\theta \right) \left(\frac{\partial \delta \hat{u}}{\partial t} - \Omega \delta \hat{v} \right) + \left[\Omega(r + u_r) + \frac{\partial u_\theta}{\partial t} \right] \left(\Omega \delta \hat{u}_r + \frac{\partial \delta \hat{v}}{\partial t} \right) + \frac{\partial \hat{w}}{\partial t} \frac{\partial \delta \hat{w}}{\partial t} \right\} d\Lambda \tag{31}$$

And

$$\delta U = \int_{\Lambda} (\sigma_{rr} \delta \varepsilon_{rr} + \sigma_{rr0} \delta \varepsilon_{rrn} + \sigma_{\theta\theta} \delta \varepsilon_{\theta\theta} + \sigma_{\theta\theta0} \delta \varepsilon_{\theta\theta n} + \sigma_{r\theta} \delta \gamma_{r\theta} + \sigma_{r\theta0} \delta \gamma_{r\theta n} + \sigma_{rz} \delta \gamma_{rz} + \sigma_{\theta z} \delta \gamma_{\theta z}) d\Lambda \tag{32}$$

where

$$\begin{Bmatrix} \sigma_{rr} \\ \sigma_{\theta\theta} \\ \sigma_{r\theta} \\ \sigma_{rz} \\ \sigma_{\theta z} \end{Bmatrix} = \begin{bmatrix} Q_{11} & Q_{12} & 0 & 0 & 0 \\ Q_{12} & Q_{22} & 0 & 0 & 0 \\ 0 & 0 & Q_{66} & 0 & 0 \\ 0 & 0 & 0 & Q_{44} & 0 \\ 0 & 0 & 0 & 0 & Q_{55} \end{bmatrix} \begin{Bmatrix} \varepsilon_{rr} \\ \varepsilon_{\theta\theta} \\ \gamma_{r\theta} \\ \gamma_{rz} \\ \gamma_{\theta z} \end{Bmatrix} \tag{33}$$

Introducing (31, 32 and 33) and (29) in (30), along with the integration by parts, results in the following equations for the translational, rotational and warping degrees of freedom.

δu :

$$\begin{aligned} \frac{N_{rr}}{r} + \frac{\partial N_{rr}}{\partial r} - \frac{N_{\theta\theta}}{r} + \frac{1}{r} \frac{\partial N_{r\theta}}{\partial \theta} + m_1 \Omega^2 u + m_f \Omega^2 \varphi^r + m_g \Omega^2 \psi^r &= m_1 \frac{\partial^2 u}{\partial t^2} - 2m_1 \Omega \frac{\partial v}{\partial t} - 2m_f \Omega \frac{\partial \varphi^\theta}{\partial t} \\ -2m_g \Omega \frac{\partial \psi^\theta}{\partial t} + m_f \frac{\partial^2 \varphi^r}{\partial t^2} + m_g \frac{\partial^2 \psi^r}{\partial t^2} \end{aligned} \tag{34}$$

δv :

$$\begin{aligned} \frac{2N_{r\theta}}{r} + \frac{\partial N_{r\theta}}{\partial r} + \frac{1}{r} \frac{\partial N_{\theta\theta}}{\partial \theta} + m_1 \Omega^2 v + m_f \Omega^2 \varphi^\theta + m_g \Omega^2 \psi^\theta &= m_1 \frac{\partial^2 v}{\partial t^2} + 2m_1 \Omega \frac{\partial u}{\partial t} - 2m_f \Omega \frac{\partial \varphi^r}{\partial t} \\ -2m_g \Omega \frac{\partial \psi^r}{\partial t} + m_f \frac{\partial^2 \varphi^\theta}{\partial t^2} + m_g \frac{\partial^2 \psi^\theta}{\partial t^2} \end{aligned} \tag{35}$$

δw :

$$N_{rr0} \frac{\partial^2 w}{\partial r^2} + \left(\frac{N_{rr0}}{r} + \frac{\partial N_{rr0}}{\partial r} + \frac{1}{r} \frac{\partial N_{r\theta0}}{\partial \theta} \right) \frac{\partial w}{\partial r} + \frac{N_{\theta\theta0}}{r^2} \frac{\partial^2 w}{\partial \theta^2} + \left(\frac{1}{r} \frac{\partial N_{r\theta0}}{\partial r} + \frac{1}{r^2} \frac{\partial N_{\theta\theta0}}{\partial \theta} \right) \frac{\partial w}{\partial \theta}$$

$$+ \frac{2N_{r\theta 0}}{r} \frac{\partial^2 w}{\partial r \partial \theta} + \frac{\partial Q_{rz}}{\partial r} + \frac{1}{r} \frac{\partial Q_{\theta z}}{\partial \theta} + \frac{Q_{rz}}{r} = m_1 \frac{\partial^2 w}{\partial t^2} \tag{36}$$

$\delta\varphi^r$:

$$\begin{aligned} \frac{\partial M_{rr}}{\partial r} + \frac{M_{rr}}{r} + \frac{1}{r} \frac{\partial M_{r\theta}}{\partial \theta} - \frac{M_{\theta\theta}}{r} - R_{rz} + m_f \Omega^2 u + m_{ff} \Omega^2 \varphi^r + m_{fg} \Omega^2 \psi^r &= m_f \frac{\partial^2 u}{\partial t^2} + m_{ff} \frac{\partial^2 \varphi^r}{\partial t^2} + m_{fg} \frac{\partial^2 \psi^r}{\partial t^2} \\ - 2m_f \Omega \frac{\partial v}{\partial t} - 2m_{ff} \Omega \frac{\partial \varphi^\theta}{\partial t} - 2m_{fg} \Omega \frac{\partial \psi^\theta}{\partial t} & \end{aligned} \tag{37}$$

$\delta\psi^r$:

$$\begin{aligned} \frac{\partial P_{rr}}{\partial r} + \frac{P_{rr}}{r} + \frac{1}{r} \frac{\partial P_{r\theta}}{\partial \theta} - \frac{P_{\theta\theta}}{r} - T_{rz} + m_g \Omega^2 u + m_{fg} \Omega^2 \varphi^r + m_{gg} \Omega^2 \psi^r &= m_g \frac{\partial^2 u}{\partial t^2} + m_{fg} \frac{\partial^2 \varphi^r}{\partial t^2} + m_{gg} \frac{\partial^2 \psi^r}{\partial t^2} \\ - 2m_g \Omega \frac{\partial v}{\partial t} - 2m_{fg} \Omega \frac{\partial \varphi^\theta}{\partial t} - 2m_{gg} \Omega \frac{\partial \psi^\theta}{\partial t} & \end{aligned} \tag{38}$$

$\delta\varphi^\theta$:

$$\begin{aligned} \frac{\partial M_{r\theta}}{\partial r} + \frac{2M_{r\theta}}{r} + \frac{1}{r} \frac{\partial M_{\theta\theta}}{\partial \theta} - R_{\theta z} + m_f \Omega^2 v + m_{ff} \Omega^2 \varphi^\theta + m_{fg} \Omega^2 \psi^\theta &= m_f \frac{\partial^2 v}{\partial t^2} + m_{ff} \frac{\partial^2 \varphi^\theta}{\partial t^2} + m_{fg} \frac{\partial^2 \psi^\theta}{\partial t^2} \\ + 2m_f \Omega \frac{\partial u}{\partial t} + 2m_{ff} \Omega \frac{\partial \varphi^r}{\partial t} + 2m_{fg} \Omega \frac{\partial \psi^r}{\partial t} & \end{aligned} \tag{39}$$

$\delta\psi^\theta$:

$$\begin{aligned} \frac{\partial P_{r\theta}}{\partial r} + \frac{2P_{r\theta}}{r} + \frac{1}{r} \frac{\partial P_{\theta\theta}}{\partial \theta} - T_{\theta z} + m_g \Omega^2 v + m_{fg} \Omega^2 \varphi^\theta + m_{gg} \Omega^2 \psi^\theta &= m_g \frac{\partial^2 v}{\partial t^2} + m_{fg} \frac{\partial^2 \varphi^\theta}{\partial t^2} + m_{gg} \frac{\partial^2 \psi^\theta}{\partial t^2} \\ + 2m_g \Omega \frac{\partial u}{\partial t} + 2m_{fg} \Omega \frac{\partial \varphi^r}{\partial t} + 2m_{gg} \Omega \frac{\partial \psi^r}{\partial t} & \end{aligned} \tag{40}$$

Corresponding natural and essential boundary conditions for the obtained equations of motion are:

$$\begin{aligned} \text{Either } u_n = n_r u + n_\theta v = 0 \quad \text{or } N_{nn} = n_r^2 N_{rr} + 2n_r n_\theta N_{r\theta} + n_\theta^2 N_{\theta\theta} = 0 \\ \text{Either } u_s = -n_\theta u + n_r v = 0 \quad \text{or } N_{ns} = (n_r^2 - n_\theta^2) N_{r\theta} + n_r n_\theta (N_{rr} - N_{\theta\theta}) = 0 \\ \text{Either } w = 0 \quad \text{or } Q_{nz} = n_r Q_{rz} + n_\theta Q_{\theta z} = 0 \\ \text{Either } \varphi_n = n_r \varphi^r + n_\theta \varphi^\theta = 0 \quad \text{or } M_{nn} = n_r^2 M_{rr} + 2n_r n_\theta M_{r\theta} + n_\theta^2 M_{\theta\theta} = 0 \\ \text{Either } \varphi_s = -n_\theta \varphi^r + n_r \varphi^\theta = 0 \quad \text{or } M_{ns} = (n_r^2 - n_\theta^2) M_{r\theta} + n_r n_\theta (M_{rr} - M_{\theta\theta}) = 0 \\ \text{Either } \psi_n = n_r \psi^r + n_\theta \psi^\theta = 0 \quad \text{or } P_{nn} = n_r^2 P_{rr} + 2n_r n_\theta P_{r\theta} + n_\theta^2 P_{\theta\theta} = 0 \\ \text{Either } \psi_s = -n_\theta \psi^r + n_r \psi^\theta = 0 \quad \text{or } P_{ns} = (n_r^2 - n_\theta^2) P_{r\theta} + n_r n_\theta (P_{rr} - P_{\theta\theta}) = 0 \end{aligned} \tag{41}$$

where

$$\begin{bmatrix} N_{rr} & M_{rr} & P_{rr} \\ N_{\theta\theta} & M_{\theta\theta} & P_{\theta\theta} \\ N_{r\theta} & M_{r\theta} & P_{r\theta} \end{bmatrix} = \int_{-\frac{h}{2}}^{\frac{h}{2}} \begin{Bmatrix} \sigma_{rr} \\ \sigma_{\theta\theta} \\ \sigma_{r\theta} \end{Bmatrix} [1 \ f \ g] dz \tag{42}$$

$$\begin{bmatrix} Q_{rz} & R_{rz} & T_{rz} \\ Q_{\theta z} & R_{\theta z} & T_{\theta z} \end{bmatrix} = \int_{-\frac{h}{2}}^{\frac{h}{2}} \begin{Bmatrix} \sigma_{rz} \\ \sigma_{\theta z} \end{Bmatrix} [1 \ f \ g] dz \tag{43}$$

The compatibility conditions for the annular plate whose coupling sector exists at $\theta = (0, 2\pi)$ can be defined such that:

$$\begin{aligned} \mu(r, 0, t) = \mu(r, 2\pi, t) \quad \text{for } \mu = (u, v, w, \varphi^r, \varphi^\theta, \psi^r, \psi^\theta) \\ Q_{nz}(r, 0, t) = Q_{nz}(r, 2\pi, t), \\ \mu_{nm}(r, 0, t) = \mu_{nm}(r, 2\pi, t), \mu_{ns}(r, 0, t) = \mu_{ns}(r, 2\pi, t) \quad \text{for } \mu = (N, M, P) \end{aligned} \tag{44}$$

Also, for the boundary conditions we have:

Clamped,

$$u_n = 0, u_s = 0, w = 0, \varphi_n = 0, \varphi_s = 0, \psi_n = 0, \psi_s = 0 \quad (45)$$

Simple supported,

$$u_n = 0, u_s = 0, w = 0, M_{nn} = 0, \varphi_s = 0, P_{nn} = 0, \psi_s = 0 \quad (46)$$

and free,

$$N_{nn} = 0, N_{ns} = 0, Q_{nz} = 0, M_{nn} = 0, M_{ns} = 0, P_{nn} = 0, P_{ns} = 0. \quad (47)$$

2.4 The TDQ algorithm for discretization

Recently, variety of numerical techniques are employed for mechanical structures with complex motion formulations. These methods, which can be used for solving differential equations, are available mostly by the name of generalized differential quadrature [62], harmonic differential quadrature [63], or mixed finite element-differential quadrature method. Thus, Differential Quadrature (DQ) is a numerical tool which is highly applicable in discretizing linear governing equations or nonlinear ones, accompanied by the corresponding boundary conditions. However, the need for a more systematic procedure in solving equations for structures—with variety of shapes, led to an extended version of DQ method called TDQM, which is capable of determining DQ weighting coefficients in such way that the discretization of both the governing equations and the corresponding boundary conditions happens in the physical domain directly.

In order to achieve this, a suitable conformal mapping is employed as follows, which is capable of analytically transforming the proposed plates (both annular and semi-annular) with eccentricity into the new geometry without eccentricity. This transformation is geometrically depicted in Fig. 3.

$$L = \frac{\hat{Z}}{c\hat{Z} + 1} + d \quad (48)$$

in which $L = r + \bar{j}\theta$ (where $\bar{j} = \sqrt{-1}$) is the complex variable of the physical domain and $\hat{Z} = \xi + \bar{j}\eta$ is taken as the complex variable of the computational domain in which the weighting coefficients are to be obtained. In Eq. 48:

$$c = \frac{\bar{e}}{\sqrt{\bar{e}^4 - 2\bar{e}^2(a^2 + b^2) + (b^2 - a^2)^2}}, d = \frac{c\hat{b}^2}{1 - (c\hat{b})^2} \quad (49)$$

The transferred domain has the inner and outer radius \hat{b} and \hat{a} , respectively; these two notations are dependent on the in-plane geometrical characteristics of the main annular model.

$$\hat{a} = \frac{\sqrt{4c^2b^2 + 1} - 1}{2c^2b}, \hat{b} = \frac{\sqrt{4c^2a^2 + 1} - 1}{2c^2a} \quad (50)$$

By inserting $L = r + \bar{j}\theta$ and $\hat{Z} = \xi + \bar{j}\eta$ in Eq. 48, the real and imaginary parts can be separated as follows:

$$r = \frac{\sqrt{[c\xi^2(cd + 1) + \xi(2cd + 1)\cos\eta + d]^2 + \xi^2\sin^2\eta}}{c^2\xi^2 + 2c\xi\cos\eta + 1} \quad (51)$$

$$\theta = \tan^{-1} \left[\frac{\xi\sin\eta}{c\xi^2(cd + 1) + \xi(2cd + 1)\cos\eta + d} \right] \quad (52)$$

The chain rule of derivative gives the following relations of transformation, which relate physical coordinates (r, θ) to the computational coordinates (ξ, η) .

$$\begin{Bmatrix} \frac{\partial\mu}{\partial r} \\ \frac{\partial\mu}{\partial\theta} \end{Bmatrix} = \begin{bmatrix} T_{11} & T_{12} \\ T_{21} & T_{22} \end{bmatrix} \begin{Bmatrix} \frac{\partial\mu}{\partial\xi} \\ \frac{\partial\mu}{\partial\eta} \end{Bmatrix} \quad (53)$$

in which μ is an arbitrary function; T_{ij} (for $i, j = 1, 2$) are obtained as follows:

$$\begin{bmatrix} T_{11} & T_{12} \\ T_{21} & T_{22} \end{bmatrix} = \begin{bmatrix} \frac{\partial r}{\partial \xi} & \frac{\partial \theta}{\partial \xi} \\ \frac{\partial r}{\partial \eta} & \frac{\partial \theta}{\partial \eta} \end{bmatrix}^{-1} \tag{54}$$

Regarding the DQM, the number of radial and circumferential grid points (in the computational domain) are taken as N_ξ and N_η , respectively. The grids are generated based on the Gauss Lobatto Chebyshev; thus we have:

$$\xi_i = \hat{b} + \frac{(\hat{a} - \hat{b})}{2} \left\{ 1 - \cos \left[\frac{(i-1)\pi}{N_\xi - 1} \right] \right\}, \quad \eta_j = \frac{\pi}{k} \left\{ 1 - \cos \left[\frac{(j-1)\pi}{N_\eta - 1} \right] \right\} \text{ for } k = \begin{cases} 1 & \text{EA} \\ 2 & \text{ESA} \end{cases}, \tag{55}$$

$i = 1, 2, \dots, N_\xi, j = 1, 2, \dots, N_\eta.$

The first-order derivatives of $\mu = (u, v, w, \phi^r, \phi^\theta, \psi^r, \psi^\theta)$ at the point (r_i, θ_j) are derived based on DQM in the physical domain. So, we have:

$$\left(\frac{\partial \mu}{\partial r} \right)_{ij} = \sum_{p=1}^{N_r=N_\xi} \sum_{q=1}^{N_\theta=N_\eta} \tilde{A}_{ijpq}^r \mu_{pq}, \quad \left(\frac{\partial \mu}{\partial \theta} \right)_{ij} = \sum_{p=1}^{N_r=N_\xi} \sum_{q=1}^{N_\theta=N_\eta} \tilde{A}_{ijpq}^\theta \mu_{pq} \tag{56}$$

in which

$$\begin{aligned} \tilde{A}_{ijpq}^r &= (T_{11})_{ij} A_{ip}^\xi \delta_{jq} + (T_{12})_{ij} \delta_{ip} A_{jq}^\eta, \\ \tilde{A}_{ijpq}^\theta &= (T_{21})_{ij} A_{ip}^\xi \delta_{jq} + (T_{22})_{ij} \delta_{ip} A_{jq}^\eta \end{aligned} \tag{57}$$

In Eq. 57, the transformed weighting coefficients \tilde{A}_{ijpq}^r and \tilde{A}_{ijpq}^θ are introduced, in which $A_{ij}^\gamma (\gamma = \xi, \eta)$ illustrate the first-order weighting coefficients along the direction of $\gamma = (\xi, \eta)$; also, δ_{ij} is Kronecker delta.

The discretization of the second-order derivatives (in the physical domain at the point (r_i, θ_j)) is formulated using the similar procedure, as follows:

$$\begin{aligned} \left(\frac{\partial^2 \mu}{\partial r^2} \right)_{ij} &= \sum_{p=1}^{N_r=N_\xi} \sum_{q=1}^{N_\theta=N_\eta} \tilde{B}_{ijpq}^r \mu_{pq}, \quad \left(\frac{\partial^2 \mu}{\partial \theta^2} \right)_{ij} = \sum_{p=1}^{N_r=N_\xi} \sum_{q=1}^{N_\theta=N_\eta} \tilde{B}_{ijpq}^\theta \mu_{pq}, \\ \left(\frac{\partial^2 \mu}{\partial r \partial \theta} \right)_{ij} &= \sum_{p=1}^{N_r=N_\xi} \sum_{q=1}^{N_\theta=N_\eta} \tilde{B}_{ijpq}^{r\theta} \mu_{pq} \end{aligned} \tag{58}$$

Including the coefficients from Eq. 57, the transformed coefficients related to the second-order derivatives are expressed such that:

$$\begin{aligned} \tilde{B}_{ijpq}^r &= \sum_{k=1}^{N_r} \sum_{l=1}^{N_\theta} \tilde{A}_{ikjl}^r \tilde{A}_{kplq}^r, \quad \tilde{B}_{ijpq}^{\theta} = \sum_{k=1}^{N_r} \sum_{l=1}^{N_\theta} \tilde{A}_{ikjl}^r \tilde{A}_{kplq}^\theta, \\ \tilde{B}_{ijpq}^{\theta} &= \sum_{k=1}^{N_r} \sum_{l=1}^{N_\theta} \tilde{A}_{ikjl}^\theta \tilde{A}_{kplq}^\theta \end{aligned} \tag{59}$$

Now, the initial displacements (\bar{u}, \bar{v}) can be discretized based on the mentioned rules of TDQM. So, we have:

$$\begin{aligned} \delta \bar{u} : \\ \sum_{p=1}^{N_r} \sum_{q=1}^{N_\theta} \left\{ \left(\frac{H_{11} \tilde{A}_{ijpq}^{rj}}{r_{ij}} + \frac{H_{66} \tilde{B}_{ijpq}^\theta}{r_{ij}^2} + H_{11} \tilde{B}_{ijpq}^{rj} - \frac{H_{22} \tilde{\delta}_{ijpq}}{r_{ij}^2} \right) \bar{u}_{pq} \right. \\ \left. + \left[- \left(\frac{H_{22}}{r_{ij}^2} + \frac{H_{66}}{r_{ij}^2} \right) \tilde{A}_{ijpq}^\theta + \frac{H_{12} \tilde{B}_{ijpq}^{r\theta}}{r_{ij}} + \frac{H_{66} \tilde{B}_{ijpq}^{r\theta}}{r_{ij}} \right] \bar{v}_{pq} \right\} = \end{aligned}$$

$$-\frac{N_{T\theta 0}}{r_{ij}} + \frac{N_{Tr0}}{r_{ij}} - m_1 \Omega^2 (r_{ij} + \bar{u}_{ij}) \tag{60}$$

$\delta \bar{v}$:

$$\sum_{p=1}^{N_r} \sum_{q=1}^{N_\theta} \left\{ \left[\left(\frac{H_{22}}{r_{ij}^2} + \frac{H_{66}}{r_{ij}^2} \right) \tilde{A}_{ipjq}^\theta + \frac{H_{12} \tilde{B}_{ipjq}^{r\theta}}{r_{ij}} + \frac{H_{66} \tilde{B}_{ipjq}^{r\theta}}{r_{ij}} \right] \bar{u}_{pq} + \left(\frac{H_{66} \tilde{A}_{ipjq}^{r_{ij}}}{r_{ij}} + \frac{H_{22} \tilde{B}_{ipjq}^\theta}{r_{ij}^2} + H_{66} \tilde{B}_{ipjq}^{r_{ij}} - \frac{H_{66} \tilde{\delta}_{ipjq}}{r_{ij}^2} \right) \bar{v}_{pq} \right\} = -m_1 \Omega^2 \bar{v}_{ij} \tag{61}$$

in which $r_{ij} = \sqrt{[c\xi_i^2(cd + 1) + \xi_i(2cd + 1) \cos \eta_j + d]^2 + \xi_i^2 \sin^2 \eta_j} / (c^2 \xi_i^2 + 2c\xi_i \cos \eta_j + 1)$. With the similar manner, the discretized form for Eqs. 34, 35, 36, 37, 38, 39 and 40 is presented as follows:

δu :

$$\begin{aligned} & \sum_{p=1}^{N_r} \sum_{q=1}^{N_\theta} \left\{ \left(\frac{H_{66} \tilde{B}_{ipjq}^\theta}{r_{ij}^2} + H_{11} \tilde{B}_{ipjq}^{r_{ij}} + \frac{H_{11} \tilde{A}_{ipjq}^{r_{ij}}}{r_{ij}} + m_1 \Omega^2 \tilde{\delta}_{ipjq} - \frac{H_{22} \tilde{\delta}_{ipjq}}{r_{ij}^2} \right) u_{pq} \right. \\ & + \left(\frac{H_{12} \tilde{B}_{ipjq}^{r\theta}}{r_{ij}} + \frac{H_{66} \tilde{B}_{ipjq}^{r\theta}}{r_{ij}} - \frac{H_{22} \tilde{A}_{ipjq}^\theta}{r_{ij}^2} - \frac{H_{66} \tilde{A}_{ipjq}^\theta}{r_{ij}^2} \right) v_{pq} \\ & + \left(\frac{H_{11} \tilde{A}_{ipjq}^{r_{ij}}}{r_{ij}} + H_{11} \tilde{B}_{ipjq}^{r_{ij}} + \frac{H_{66} \tilde{B}_{ipjq}^\theta}{r_{ij}^2} + m_f \Omega^2 \tilde{\delta}_{ipjq} - \frac{H_{22} \tilde{\delta}_{ipjq}}{r_{ij}^2} \right) \phi_{pq}^r + \\ & \left(\frac{H_{11} \tilde{A}_{ipjq}^{r_{ij}}}{r_{ij}} + H_{11} \tilde{B}_{ipjq}^{r_{ij}} + \frac{H_{66} \tilde{B}_{ipjq}^\theta}{r_{ij}^2} + m_g \Omega^2 \tilde{\delta}_{ipjq} - \frac{H_{22} \tilde{\delta}_{ipjq}}{r_{ij}^2} \right) \psi_{pq}^r + \\ & \left. \left(\frac{H_{12} \tilde{B}_{ipjq}^{r\theta}}{r_{ij}} + \frac{H_{66} \tilde{B}_{ipjq}^{r\theta}}{r_{ij}} - \frac{H_{22} \tilde{A}_{ipjq}^\theta}{r_{ij}^2} - \frac{H_{66} \tilde{A}_{ipjq}^\theta}{r_{ij}^2} \right) \phi_{pq}^\theta + \left(\frac{H_{12} \tilde{B}_{ipjq}^{r\theta}}{r_{ij}} + \frac{H_{66} \tilde{B}_{ipjq}^{r\theta}}{r_{ij}} - \frac{H_{22} \tilde{A}_{ipjq}^\theta}{r_{ij}^2} - \frac{H_{66} \tilde{A}_{ipjq}^\theta}{r_{ij}^2} \right) \psi_{pq}^\theta \right\} \\ & = m_1 \left(\frac{\partial^2 u}{\partial t^2} \right)_{ij} - 2m_1 \Omega \left(\frac{\partial v}{\partial t} \right)_{ij} - 2m_f \Omega \left(\frac{\partial \phi^r}{\partial t} \right)_{ij} - 2m_g \Omega \left(\frac{\partial \psi^r}{\partial t} \right)_{ij} + m_f \left(\frac{\partial^2 \phi^r}{\partial t^2} \right)_{ij} + m_g \left(\frac{\partial^2 \psi^r}{\partial t^2} \right)_{ij} \end{aligned} \tag{62}$$

Note that only δu is shown above; the rest of the discretized equations can be pursued in Appendix B.

One is able to compress the motion equations and the boundary conditions into a matrix. Hence, for the initial displacements Eq. 60 and 61, we have:

$$\begin{bmatrix} K_{\bar{u}\bar{u}} & K_{\bar{u}\bar{v}} \\ K_{\bar{v}\bar{u}} & K_{\bar{v}\bar{v}} \end{bmatrix} \begin{Bmatrix} \bar{u} \\ \bar{v} \end{Bmatrix} = \begin{Bmatrix} F_{\bar{u}} \\ F_{\bar{v}} \end{Bmatrix} \tag{63}$$

where $(K_{\bar{u}\bar{u}}, K_{\bar{u}\bar{v}}, K_{\bar{v}\bar{u}}, K_{\bar{v}\bar{v}})$ are the initial stiffness elements and $(F_{\bar{u}}, F_{\bar{v}})$ are the body forces. In addition, the equations of motion in Eqs. 62, 68, 69, 70, 71, 72 and 73 are presented as follows:

$$[K_{db}] \{U_b\} + [K_{dd}] \{U_d\} + [M] \left\{ \frac{d^2 U_d}{dt^2} \right\} = 0 \tag{64}$$

where $\{U_i\} = \left[\{u_i\}^T \{v_i\}^T \{w_i\}^T \{\phi_i^r\}^T \{\phi_i^\theta\}^T \{\psi_i^r\}^T \{\psi_i^\theta\}^T \right]^T$ with $i = b$ and d . Also, $[K_{ij}]$ and $[M]$ with $(i, j = b, d)$ are the stiffness and mass matrices, respectively. Above, the subscripts b and d are short forms for the boundary and the domain, respectively. Also, for the boundary conditions we have:

$$[K_{bb}] \{U_b\} + [K_{bd}] \{U_d\} = 0 \tag{65}$$

By replacing Eq. 65 into 64, it is possible to omit U_b , so that the following algebraic eigenvalue problem emerges from which the natural frequencies of the FG-GRC eccentric annular or semi-annular plate, as well as its mode shapes, can be obtained.

$$([K] - \omega_i^2 [M]) \{\hat{U}_d\} = 0, \text{ for } i = 1, 2, 3, \dots \tag{66}$$

In Eq. 66, $[K] = [K_{dd}] - [K_{db}][K_{bb}]^{-1}[K_{bd}]$. Additionally, it is important to mention that Eq. 66 is derived based on the harmonic essence of the motion and as a result, ω_i for $i = 1, 2, 3, \dots$ is the i th natural frequency of the plate and $\{\hat{U}_d\}$ are the corresponding mode shape of the proposed oscillating model, respectively.

Table 1 Comparing the convergence rate of a C–C–F–F nonrotating and nonporous FG–GRC–ESA plate with uniform distribution of graphene platelets at various temperature difference; ($a = 1$ m, $h/a = 0.01$, $b/a = 0.3$, $\Lambda_{GPL} = 0.01$). The frequencies ω_i for $i = 1,2,3$ and 4 are in Hz, and the temperature difference ΔT is in Celsius

$N_r = N_\theta$		$\bar{e}/a = 0$				$\bar{e}/a = 0.2\bar{e}/a = 0.2$			
		ω_1	ω_2	ω_3	ω_4	ω_1	ω_2	ω_3	ω_4
11	$\Delta T = 0$	108.031	110.431	119.033	136.860	65.2650	89.3510	124.987	172.766
13		108.068	110.414	119.149	136.926	72.1222	103.952	137.629	167.075
17		108.120	110.380	119.299	136.909	70.3181	100.857	136.300	172.633
21		108.147	110.364	119.377	136.911	69.9903	100.144	136.065	172.428
23		108.155	110.359	119.400	136.910	70.2780	100.190	136.115	172.562
25		108.162	110.353	119.418	136.909	70.4151	100.234	136.165	172.677
27		108.166	110.348	119.431	136.906	70.4262	100.234	136.179	172.735
ABAQUS		108.591	110.434	119.840	137.362	69.9174	110.173	136.280	172.982
11	$\Delta T = 15$	84.3396	87.9572	94.6199	110.479	49.2370	63.7475	95.2978	143.063
13		84.3614	87.9758	94.8247	110.873	51.4311	81.0877	116.248	140.787
17		84.3788	87.985	95.0144	110.847	50.0796	76.3176	108.887	143.936
21		84.3836	87.9752	95.0846	110.835	49.5281	75.2894	108.831	144.498
23		84.3813	87.9651	95.1031	110.834	49.8280	75.2875	108.826	144.551
25		84.3811	87.9547	95.1028	110.804	49.9812	75.3227	108.878	144.663
27		84.3727	87.9547	95.1158	110.801	49.9948	75.3101	108.888	144.698
ABAQUS		83.9612	87.5201	94.8281	110.702	49.6940	75.7541	145.793	168.894
11	$\Delta T = 30$	42.2231	49.5534	60.3905	74.8027	40.5229	40.5229	103.966	138.285
13		42.3110	49.0925	60.5680	77.1551	38.4899	86.1322	113.064	133.848
17		42.2824	49.1711	60.6786	76.7369	34.7174	70.1274	106.137	141.852
21		42.2779	49.1687	60.6969	76.6833	30.9097	69.6030	108.012	140.598
23		42.2699	49.1494	60.6842	76.6701	30.8895	69.5521	107.954	139.401
25		42.2912	49.1471	60.6802	76.6124	30.9144	69.6137	108.088	138.996
27		42.2177	49.1147	60.6875	76.5820	30.8562	69.6088	108.084	138.738
ABAQUS		42.5480	49.3912	60.9391	77.0460	32.3231	71.0642	109.830	141.402

Table 2 Comparing the convergence rate of a C–F nonporous FG–GRC annular plate with uniform distribution of graphene platelets at various rotating speed Ω (rad/s); ($a = 1$ m, $h/a = 0.01$, $b/a = 0.3$, $\Delta T = 0$, $\Lambda_{GPL} = 0.01$). The frequencies ω_i for $i = 1,2,3$ and 4 are in Hz, and the temperature difference ΔT is in Celsius

$N_r = N_\theta$	$\Omega = 0$				$\Omega = 100$				
	ω_1	ω_2	ω_3	ω_4	ω_1	ω_2	ω_3	ω_4	
11	15.9047	15.9048	16.1195	19.2282	23.9871	25.2618	25.2619	30.9973	
13	15.8485	15.8486	16.1046	19.0365	23.9605	25.2052	25.2052	30.8656	
17	15.8317	15.8317	16.1060	18.9609	23.9616	25.1942	25.1942	30.8162	
21	15.8272	15.8272	16.1073	18.9343	23.9634	25.1929	25.1929	30.8011	
23	15.8251	15.8251	16.1070	18.9256	23.9629	25.1915	25.1915	30.7959	
25	15.8226	15.8226	16.1061	18.9180	23.9615	25.1894	25.1894	30.7911	
27	15.8196	15.8196	16.1046	18.9109	23.9593	25.1866	25.1866	30.7861	
ABAQUS		15.8791	15.8790	16.3122	18.6823	23.9950	23.1352	25.1361	30.5834
$N_r = N_\theta$	$\Omega = 150$				$\Omega = 200$				
	ω_1	ω_2	ω_3	ω_4	ω_1	ω_2	ω_3	ω_4	
11	31.0032	33.3734	33.3735	41.2065	38.6240	42.1074	42.1075	52.2296	
13	30.9571	33.3020	33.3020	41.0906	38.5431	42.0059	42.0059	52.1122	
17	30.9563	33.2913	33.2913	41.0491	38.5376	41.9919	41.9919	52.0722	
21	30.9585	33.2914	33.2914	41.0387	38.5402	41.9929	41.9929	52.0647	
23	30.9579	33.2903	33.2903	41.0349	38.5393	41.9919	41.9919	52.0617	
25	30.9560	33.2882	33.2882	41.0310	38.5370	41.9896	41.9896	52.0583	
27	30.9532	33.2851	33.2851	41.0267	38.5335	41.9862	41.9862	52.0543	
ABAQUS		29.3210	32.9321	32.9335	40.9371	38.3570	41.7962	41.7961	51.8294

Table 3 Comparison study of the fundamental dimensionless frequency $\bar{\omega} = \sqrt[4]{\omega^2 \frac{12m_1 a^4(1-\nu^2)}{Eh^3}} [4] \omega^2 \frac{12m_1 a^4(1-\nu^2)}{Eh^3}$ for the EA plates in terms of various boundary conditions and eccentricity parameter; ($b/a = 0.3, h/a = 0.01, \Lambda_{GPL} = 0, e_0 = 0, \nu = 0.3, \Delta T = 0, \Omega = 0$)

Method	C-C			C-F		
	$\bar{e}/a = 0$	$\bar{e}/a = 0.1$	$\bar{e}/a = 0.2$	$\bar{e}/a = 0$	$\bar{e}/a = 0.1$	$\bar{e}/a = 0.2$
Present	6.7287	6.0884	5.5317	2.5618	2.2939	2.0635
FSDT [26]	6.7285	6.0884	5.5098	2.5590	2.2986	2.0660
CPT [65]	6.730	6.092	5.514	2.515	2.299	2.068
ABAQUS	6.7421 (4564)*	6.0949 (4484)	5.5136 (4446)	2.5601 (4564)	2.2985 (4484)	2.0659 (4446)

*Total number of (S4R) elements

Table 4 Fundamental frequency (Hz) of an FG-GRC-ESA plate; ($a = 1 \text{ m}, h/a = 0.01, b/a = 0.3, \Omega = 100 \text{ rad/s}, \Lambda_{GPL} = 0.01$)

	C-C-C-C			C-C-F-F		
	$\bar{e}/a = 0$	$\bar{e}/a = 0.1$	$\bar{e}/a = 0.2$	$\bar{e}/a = 0$	$\bar{e}/a = 0.1$	$\bar{e}/a = 0.2$
$e_0 = 0$						
Type-A	125.043	115.923	105.257	119.265	95.5723	77.1887
Type-B	110.836	102.760	93.3004	105.570	84.4663	67.6660
Type-C	113.020	104.766	95.1104	107.685	86.1751	69.1288
Type - I, $e_0 = 0.5$						
Type-A	123.070	114.114	103.616	117.311	93.8425	75.9727
Type-B	109.928	101.942	92.5743	104.673	83.6951	67.4008
Type-C	112.852	104.616	94.9800	107.523	85.9882	69.3668
Type - II, $e_0 = 0.5$						
Type-A	112.702	104.534	94.9483	107.380	85.9651	69.2851
Type-B	99.8229	92.5876	84.0934	94.9793	75.9651	60.7334
Type-C	102.571	95.1019	86.3551	97.6584	78.0945	62.5603

Table 5 Fundamental frequency (Hz) of an FG-GRC-EA plate (Type-A) with the porosity being symmetrically distributed at various rotating speed Ω (rad/s); ($a = 1 \text{ m}, h/a = 0.01, b/a = 0.3, \bar{e}/a = 0.2, e_0 = 0.5$). The temperature difference ΔT is in Celsius

ΔT	B.Cs.	$\Lambda_{GPL} = 0.015$			$\Lambda_{GPL} = 0.02$		
		$\Omega = 50$	$\Omega = 100$	$\Omega = 200$	$\Omega = 50$	$\Omega = 100$	$\Omega = 200$
5°	C - C	214.593	214.344	213.345	233.990	233.760	232.835
	C - S	161.391	160.549	157.135	175.996	175.222	172.087
	C - F	43.1334	46.7066	58.6353	46.7706	50.0914	61.4184
10°	C - C	210.719	210.465	209.447	230.147	229.913	228.972
	C - S	156.615	155.747	152.223	171.261	170.464	167.238
	C - F	43.4245	46.9739	58.8432	47.0872	50.3855	61.6531

3 Numerical results

In this section, the information regarding the free vibration of the FG-GRC plate, along with a complete parameter study, is provided in diverse ways. To apply the numerical approach, the following values are assumed for both the geometric parameters and material properties of the graphene platelets (according to Yas and Rahimi [64]).

$$GPLs \begin{cases} l_{GPL} = 2.5 \mu\text{m}, & w_{GPL} = 1.5 \mu\text{m}, & t_{GPL} = 1.5 \text{ nm}, \\ \rho_{GPL} = 1062.5 \text{ Kg m}^{-3}, & E_{GPL} = 1.01 \text{ TPa}, & \nu_{GPL} = 0.186, & \alpha_{GPL} = -3.75 \times 10^{-6} \text{ K}^{-1} \end{cases}$$

In addition, the polymer matrix is made of copper with the following material properties in the room temperature [64].

$$\text{Matrix} \{ \rho_m = 8960 \text{ Kg m}^{-3}, E_m = 130 \text{ GPa}, \nu_m = 0.34, \alpha_m = 17 \times 10^{-6} \text{ K}^{-1}$$

Table 6 Fundamental frequency (Hz) of a rotating FG-GRC-EA plate (Type-A) with the porosity being asymmetrically distributed; ($a = 1$ m, $\Omega = 100$ rad/s, $\Delta T = 10^\circ$, $e_0 = 0.5$)

Λ_{GPL}	h/a	$\bar{e}/b = 0.2$			$\bar{e}/b = 0.4$		
		$b/a = 0.1$	$b/a = 0.2$	$b/a = 0.4$	$b/a = 0.1$	$b/a = 0.2$	$b/a = 0.4$
0.5%	0.01	8.40770	19.2577	50.2112	8.08750	14.1304	36.0849
	0.05	174.533	215.445	337.339	170.391	201.065	278.594
	0.1	333.460	409.410	625.208	326.092	383.817	523.672
1%	0.01	15.4421	28.5898	61.5411	13.3555	23.9805	45.9820
	0.05	200.418	247.278	386.678	195.680	230.833	319.551
	0.1	380.570	467.168	712.125	372.247	438.133	597.152
2%	0.01	28.3517	41.6923	79.6884	26.5737	36.7627	61.390
	0.05	243.424	300.183	468.724	237.699	280.304	387.641
	0.1	458.795	563.125	856.758	448.886	528.352	719.320

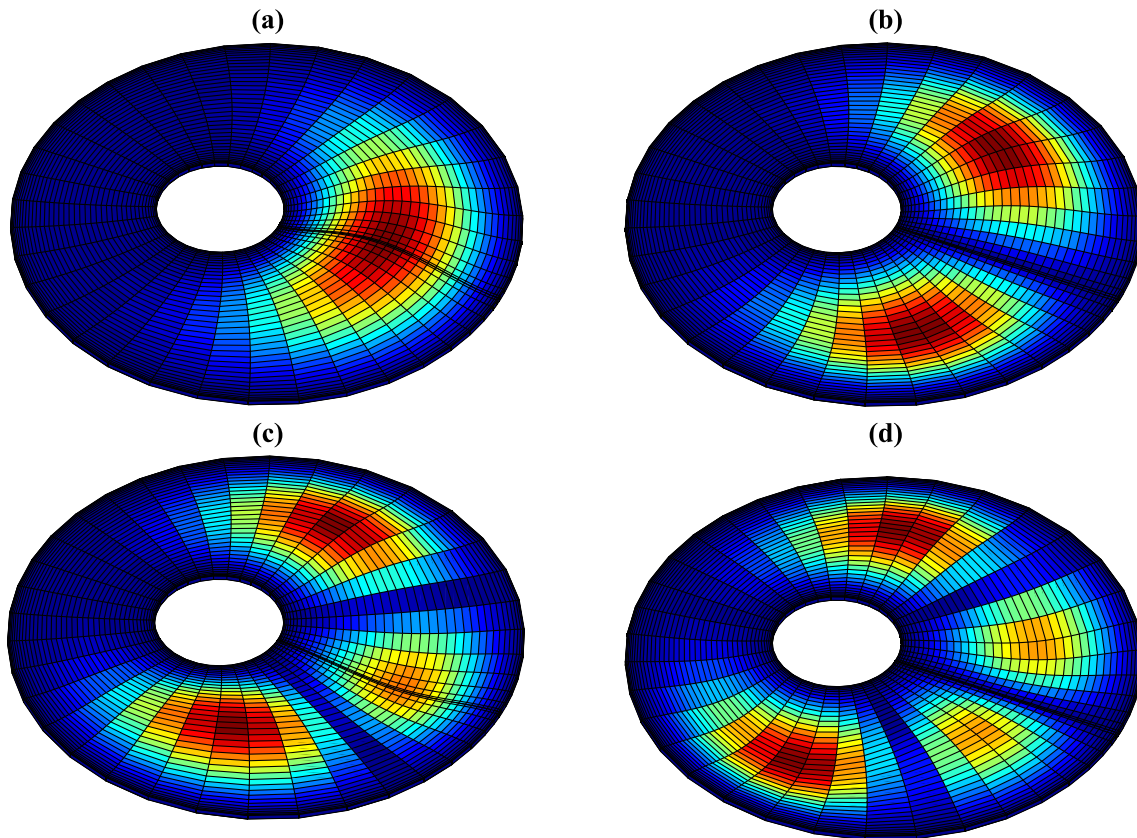


Fig. 4 Mode shapes of a C - C porous FG-GRC-EA plate, with symmetrical dispersion of graphene platelets (Type-A) and porosity (Type-I); ($a = 1$ m, $h/a = 0.01$, $b/a = 0.3$, $\bar{e}/a = 0.2$, $\Omega = 0$, $\Delta T = 0$, $e_0 = 0.5$, $\Lambda_{GPL} = 0.01$, $N_r = N_\theta = 43$); **a** first mode, **b** second mode, **c** third mode and **d** fourth mode

In the presented study, a complete eccentric annular and half-circle eccentric sector plate (semi-annular) are discussed. The boundary condition of the annular plate is identified using the two initials of the inner and outer boundary (arc) conditions; for example, the boundary condition for an EA plate with clamped inner arc and free outer arc is noted as C - F. The first two letter of the boundary condition for the ESA plate can also be noted with the similar manner; in addition, the notation is followed by the initials related to the conditions at $\theta = 0$ and $\theta = \pi$, respectively. Only then the ESA plate's boundary condition is fully identified. By means of example, for an ESA plate with clamped inner semicircle, free outer semicircle, simple boundary at $\theta = 0$ and free boundary at $\theta = \pi$, the boundary condition is noted as C-F-S-F.

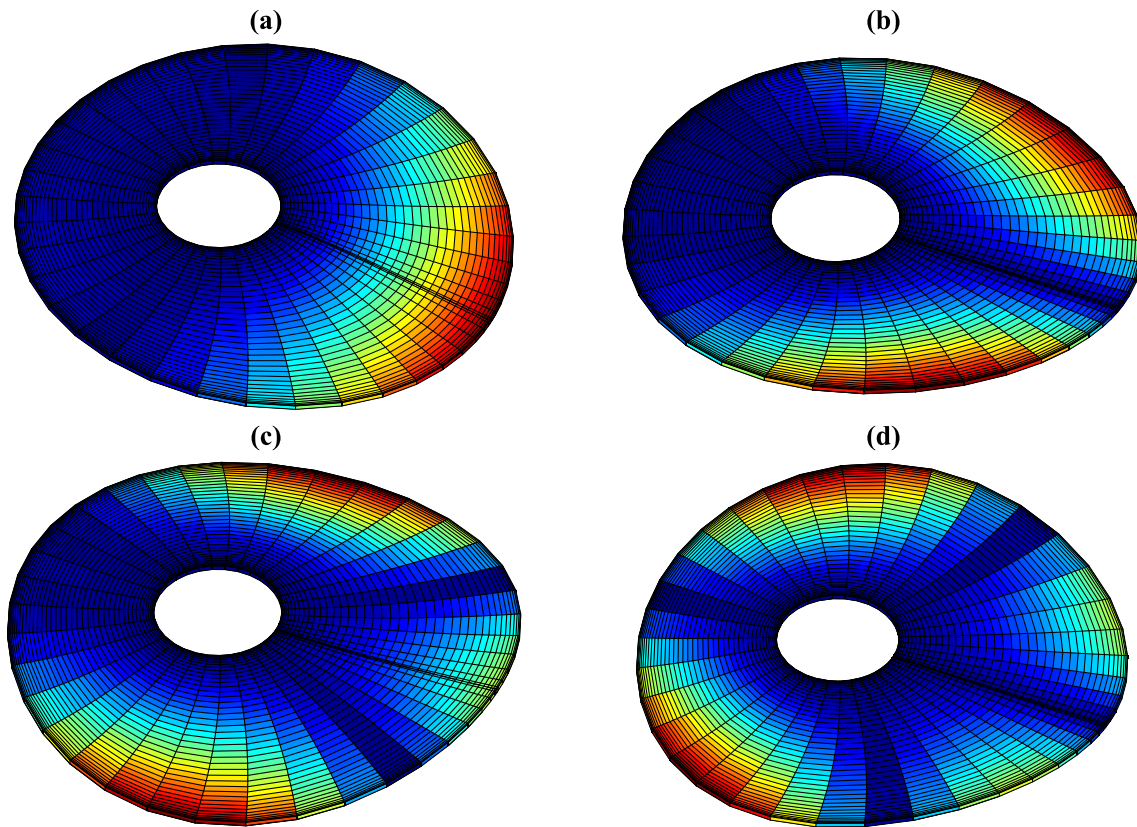


Fig. 5 Mode shapes of a C - F porous FG-GRC-EA plate, with symmetrical dispersion of graphene platelets (Type-A) and porosity (Type-I); ($a = 1$ m, $h/a = 0.01$, $b/a = 0.3$, $\bar{e}/a = 0.2$, $\Omega = 0$, $\Delta T = 0$, $e_0 = 0.5$, $\Lambda_{GPL} = 0.01$, $N_r = N_\theta = 43$); **a** first mode, **b** second mode, **c** third mode and **d** fourth mode

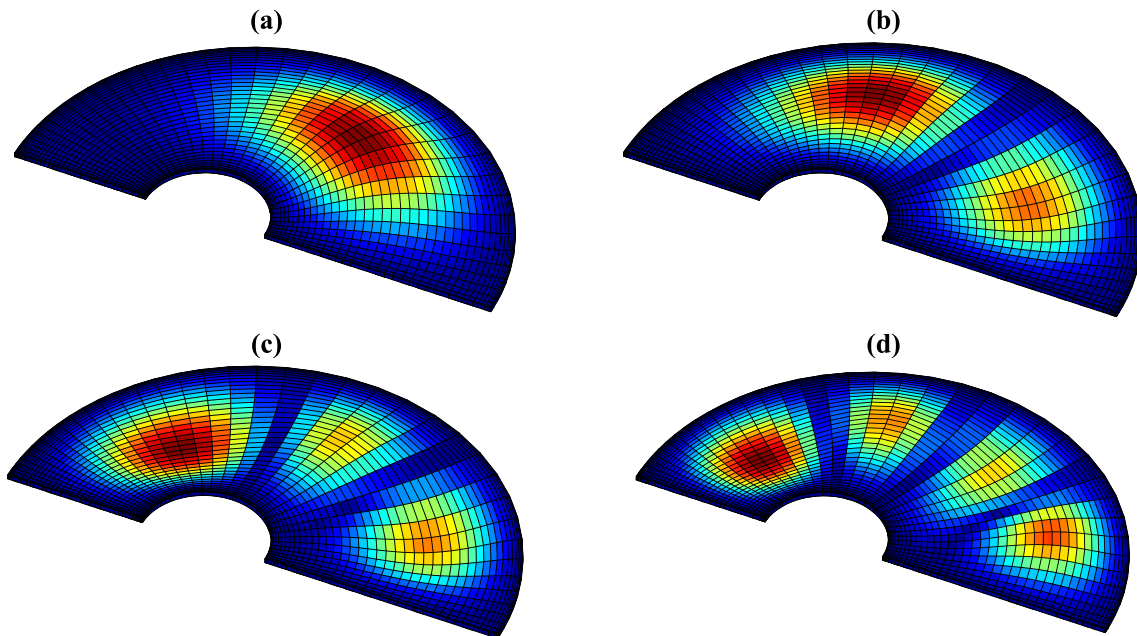


Fig. 6 Mode shapes of a C - C - C - C porous FG-GRC-ESA plate, with symmetrical dispersion of graphene platelets (Type-A) and porosity (Type-I); ($a = 1$ m, $h/a = 0.01$, $b/a = 0.3$, $\bar{e}/a = 0.2$, $\Omega = 0$, $\Delta T = 0$, $e_0 = 0.5$, $\Lambda_{GPL} = 0.01$, $N_r = N_\theta = 43$); **a** first mode, **b** second mode, **c** third mode and **d** fourth mode

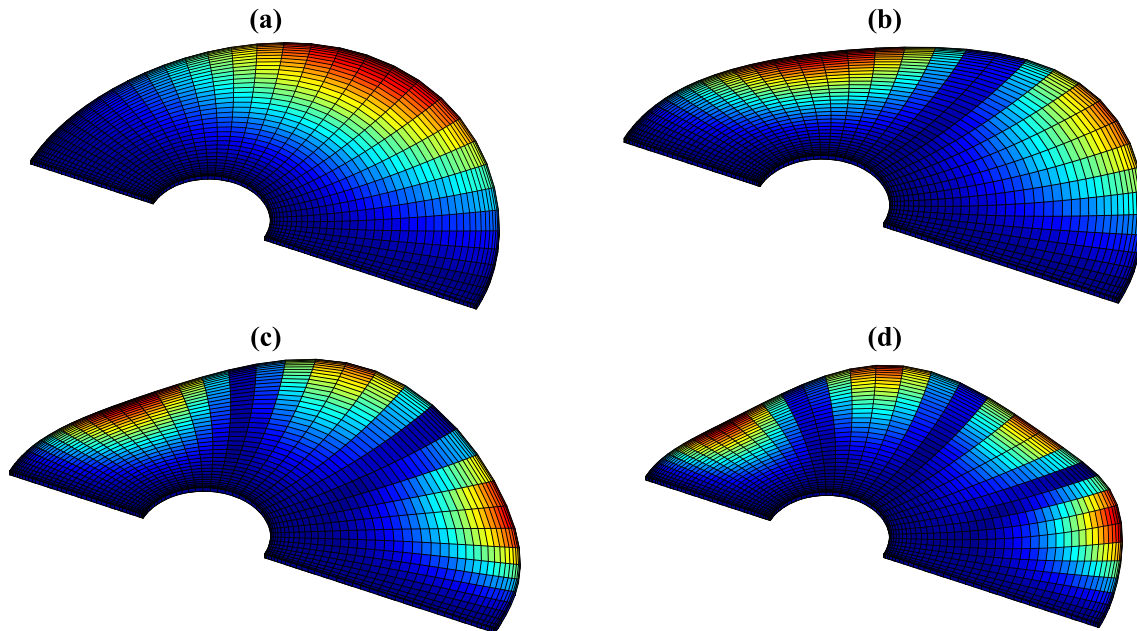


Fig. 7 Mode shapes of a C - F - C - C porous FG-GRC-ESA plate, with symmetrical dispersion of graphene platelets (Type-A) and porosity (Type-I); ($a = 1$ m, $h/a = 0.01$, $b/a = 0.3$, $\bar{e}/a = 0.2$, $\Omega = 0$, $\Delta T = 0$, $e_0 = 0.5$, $\Lambda_{GPL} = 0.01$, $N_r = N_\theta = 43$); **a** first mode, **b** second mode, **c** third mode and **d** fourth mode

In Table 1, the convergence of the natural frequencies (Hz) of an ESA plate is investigated. The authenticity of the results is established using the numerical software suite called ABAQUS, whose computational analysis is performed based on finite element methods. The convergent simulation's results are conducted using 1564 elements whose type is chosen to be 'S4RT'. The simulation has been carried out to verify the accuracy of the problem in a limited case (uniform distribution of GPLs) with the presence of thermal environment. Only the temperature difference is considered, and the rotating is assumed to be zero. For this purpose, the solver "coupled temp-displacement (steady-state)" is used. After applying each of this effect, a frequency analysis is performed on the ESA plate to calculate the frequencies of the system under the applied conditions. The model is considered neither porous nor revolving. However, the graphene is distributed uniformly based on Type-C (Eq. 8) and the boundary condition is introduced as C-C-F-F. Table 1 contains the data for the first four natural frequencies, which are in good agreement with those obtained from ABAQUS—either with ($\bar{e}/a = 0.2$) or without ($\bar{e}/a = 0$) eccentricity; this is also applied to those results when ΔT varies from 0 to 15, and then 30 degrees. The rate of convergence is considered to be good—based on the given number of node—although for higher frequencies the rate of convergence seems to decrease slightly when the eccentricity appears ($\bar{e}/a = 0.2$). Overall, the natural frequencies, especially the fundamental frequencies, decline when the eccentricity or the temperature difference increases.

Table 2 shows the convergence of the natural frequencies (Hz) of an annular plate with rising rotating speed when the temperature difference ΔT , and the eccentricity \bar{e} , are assumed zero. This rise in rotating speed causes the natural frequencies to increase. What is more, the given results are in good agreement with those obtained from ABAQUS—using the element type 'S4R'; nonetheless, the total number of elements for the annular plate to have yielded convergent results is 4564. Another simulation has been conducted to verify the accuracy of the problem in which the rotating speed is taken into account, while the temperature difference is zero. In the loading part of the software, a distributed uniform centrifugal force is defined as rotational body force to evaluate the rotating effect on the annular plate. Next, a further frequency analysis is simulated on the annular plate.

Regarding the validation of the proposed method, the results of the non-dimensional fundamental frequency are compared with two sets of data from the literature [34, 65], and those obtained from simulation using ABAQUS (with the prescribed number and type of elements), are presented in Table 3. The comparison is performed for two different boundary conditions, along with various values for eccentricity parameter. Eventually, it is obviously confirmed that results of the current study are in close agreement with the other approaches.

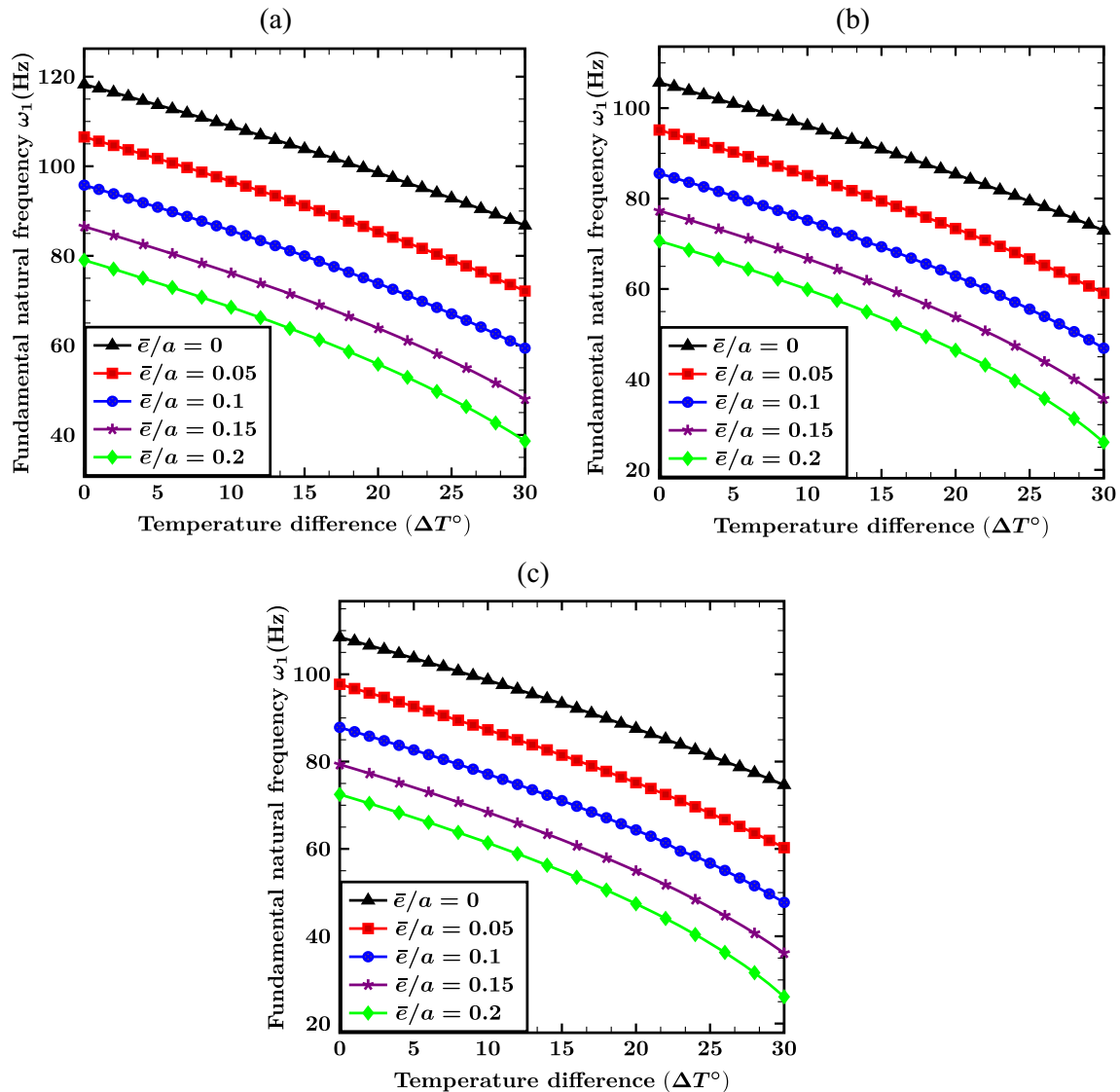


Fig. 8 The influence of temperature difference and eccentricity on the fundamental natural frequency of a rotating FG-GRC-EA plate with symmetrical porosity (Type-I) and C-C boundary conditions; the temperature difference ΔT is in Celsius. ($a = 1$ m, $h/a = 0.01$, $b/a = 0.3$, $\Omega = 100$ rad/s, $e_0 = 0.5$, $\Lambda_{GPL} = 0.01$); **a** Type-A, **b** Type-B and **c** Type-C

In Table 4, the fundamental frequency (Hz) of a rotating ESA plate in variety of circumstances under two different boundary conditions is investigated. It is deduced from Table 4 that for both of the presented boundary conditions, the increase in the eccentricity parameter \bar{e} has led to the drop in frequency regardless of the graphene distribution. This is also true when the porosity is included in the investigations. Additionally, significant reduction in the fundamental frequency is observed when the distribution of the porosity varies from the symmetrical pattern (Type-I) to the asymmetrical one (Type-II). The role of graphene distribution is also crucial when identifying the natural frequencies. It can be seen that the lowest value and the highest in each set of data belong to the Type-B (whose pattern is considered non-uniform and asymmetrical) and Type-A (with non-uniform, yet symmetrical distribution), respectively.

In Table 5, the fundamental frequency (Hz) of the EA plate with porosity Type-I and graphene Type-A is presented. It is inferred from Table 5 that by increasing the volume fraction Λ_{GPL} , the frequency for the corresponding rotating speed adds up. On the other side, the rise in ΔT mostly affects the boundary conditions C-C and C-S, whereas its influence on C-F is subtle. In contrast, the rise in Ω appears to have the major effect on the boundary condition C-F, rather than the other two. In Table 6, changes in fundamental frequency (Hz) of

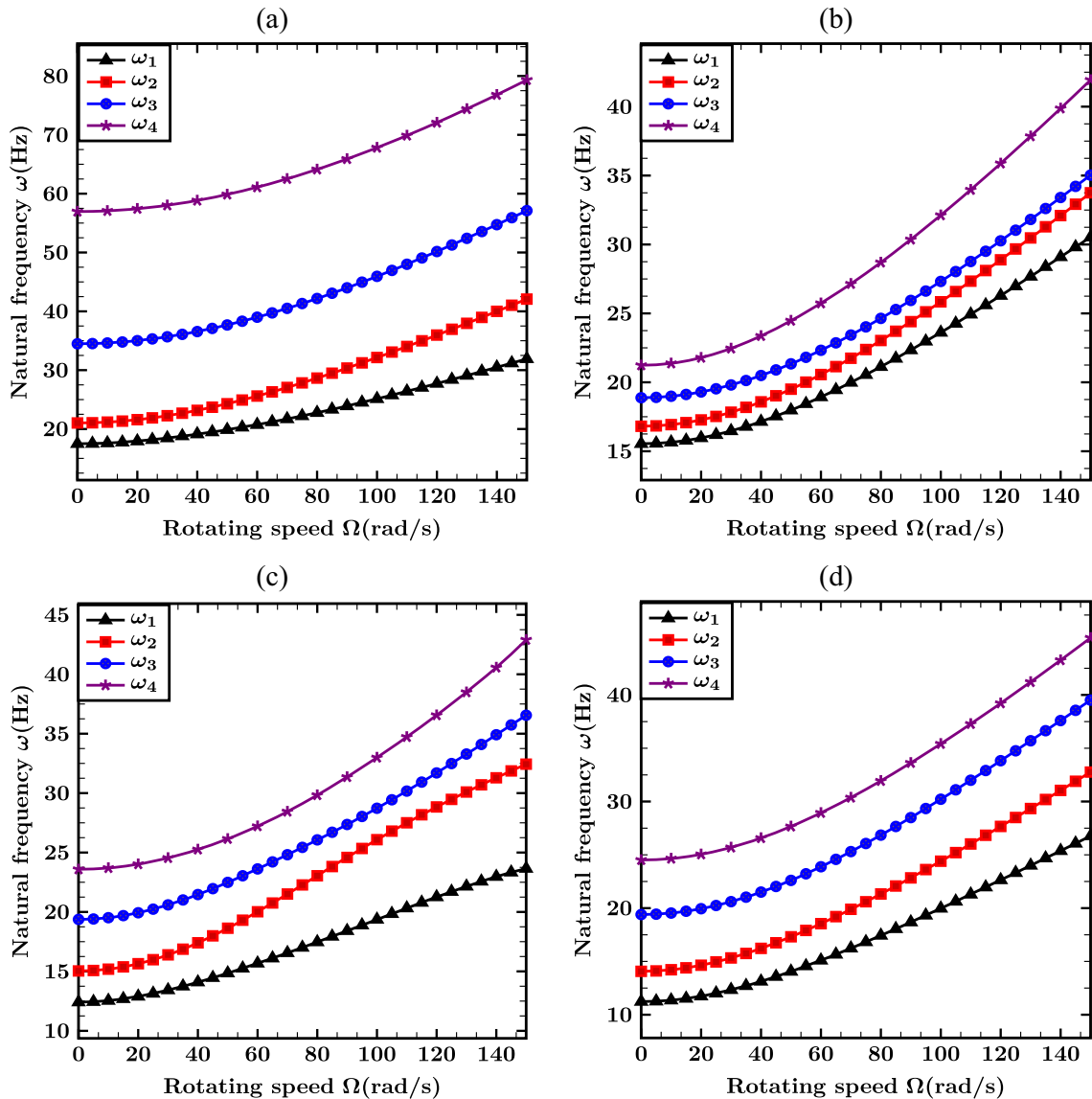


Fig. 9 The influence of rotating speed (rad/s) on the first four natural frequencies of an FG-GRC-EA plate with C-F boundary condition and symmetrical dispersion of porosity (Type-I) and graphene platelets (Type-A); ($a = 1$ m, $h/a = 0.01$, $b/a = 0.3$, $\Delta T = 0$, $e_0 = 0.2$, $\Lambda_{GPL} = 0.01$); **a** $\bar{e}/a = 0$, **b** $\bar{e}/a = 0.05$, **c** $\bar{e}/a = 0.15$ and **d** $\bar{e}/a = 0.2$

a clamped-simple rotating EA plate in terms of the various geometrical parameters are presented. The porosity and the graphene dispersion are considered asymmetrical and symmetrical, respectively. Accordingly, it is clear that the growth in plate's thickness h causes the natural frequency to rise; similarly, the same phenomenon happens when the volume fraction Λ_{GPL} changes from 0.5 to 2 percent. On the other hand, Table 6 displays a vivid decline of the natural frequency when either the inner radius shrinks, or the outer radius enlarges. Moreover, when the off-center hole is relocated to a farther distance from the center, the frequency drops.

The first four mode shapes of a porous FG-GRC-EA plate are displayed in Figs. 4 and 5. The model in Figs. 4 and 5 has symmetrical dispersion of graphene and porosity. The boundary conditions vary from Fig. 4 (C-C) to Fig. 5 (C-F). Similar assumptions are made in order to, graphically, express the first four mode shapes of a porous FG-GRC-EA plate (Figs. 6 and 7). The applied boundary conditions are C-C-C-C for Fig. 6 and C-F-C-C for Fig. 7. In Fig. 8, the variation of the fundamental natural frequency (Hz) versus temperature difference ΔT is presented for a rotating FG-GRC-EA plate, which has C-C boundary condition and Type-I porosity. As we can see in Fig. 8, the growth in temperature difference causes the fundamental frequency to

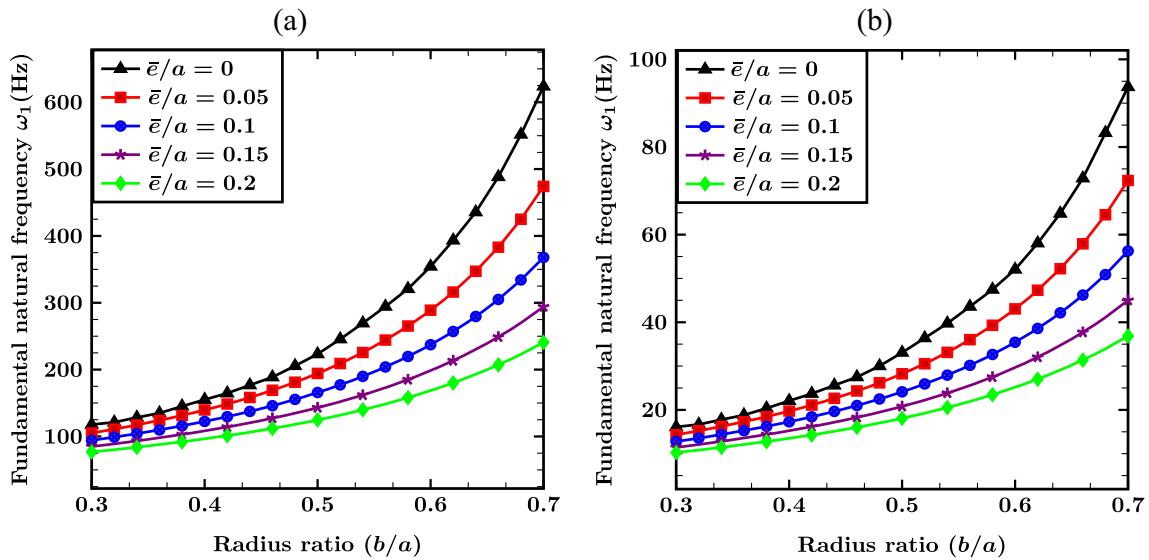


Fig. 10 The influence of the geometry on the fundamental natural frequency of a nonrotating FG-GRC-ESA plate with symmetrical dispersion of porosity (Type-I) and graphene platelets (Type-A); the temperature difference ΔT is in Celsius. ($a = 1$ m, $h/a = 0.01$, $\Delta T = 0$, $\Omega = 0$, $e_0 = 0.5$, $\Lambda_{GPL} = 0.01$); **a** C-C-F-F and **b** C-F-F-F

drop, regardless of the change in the distribution of graphene platelets. Furthermore, increasing the eccentricity reduces the fundamental frequency. When it comes to the influence of graphene platelets, one is able to see that distribution Type-A marks higher range of fundamental frequencies in comparison with Type-B and Type-C.

In Fig. 9, the effect of the rotating speed on the first four natural frequencies of an FG-GRC-EA plate is investigated. For the given C-F boundary condition, the rise in rotating speed Ω (rad/s) appears to have increased all the four natural frequencies. Another major point is that the third and fourth natural frequencies experience a significant drop when the eccentric parameter varies from zero to a small amount ($\bar{e}/a = 0.05$); however, once the eccentricity continues to grow, the third and fourth natural frequencies tend to increase. Nevertheless, this is not the case for the first and second frequencies since gradual decrease is recorded for both when the eccentricity increases.

Figure 10 illustrates the variation of the fundamental natural frequency for a nonrotating ESA plate versus the radius ratio (b/a)—which is ratio of the inner radius to the outer radius—for two different boundary conditions. The fundamental natural frequency rises as the consequence of increasing the size of the clamped inner semicircle. In addition, steady rise in eccentricity results in the decline of fundamental frequency. This decline is shown to be more noticeable for bigger radius ratios.

In Fig. 11, the four natural frequencies for a nonrotating FG-GRC-ESA plate are presented. These frequencies vary due to the change in thickness ratio (h/a), as well as the temperature difference ΔT . Although increasing the temperature was known to decrease the natural frequencies, this effect is reduced at larger thickness ratios; that is, the effect of temperature on the natural frequencies is more substantial when the thickness ratio is small, especially for the first mode. However, as the modes get higher, the impact of temperature diminishes even for small thickness ratios.

4 Conclusion

The current paper analyzed the free oscillation of rotating FG annular and semi-annular plates with off-centered circular cut-outs and various boundary conditions in a thermal environment. Porosity is included in the model with symmetrical and asymmetrical dispersions along the thickness of the plate; the structure is reinforced with GPLs based on three different types, including non-uniform (symmetrical and asymmetrical) and uniform. These assumptions lead to complex equations derived using Hamilton's principles, and then tackled utilizing the systematic and efficient transformed differential quadrature method (TDQM). Diverse numerical results certified that the developed method has fast convergence rate and is highly accuracy.

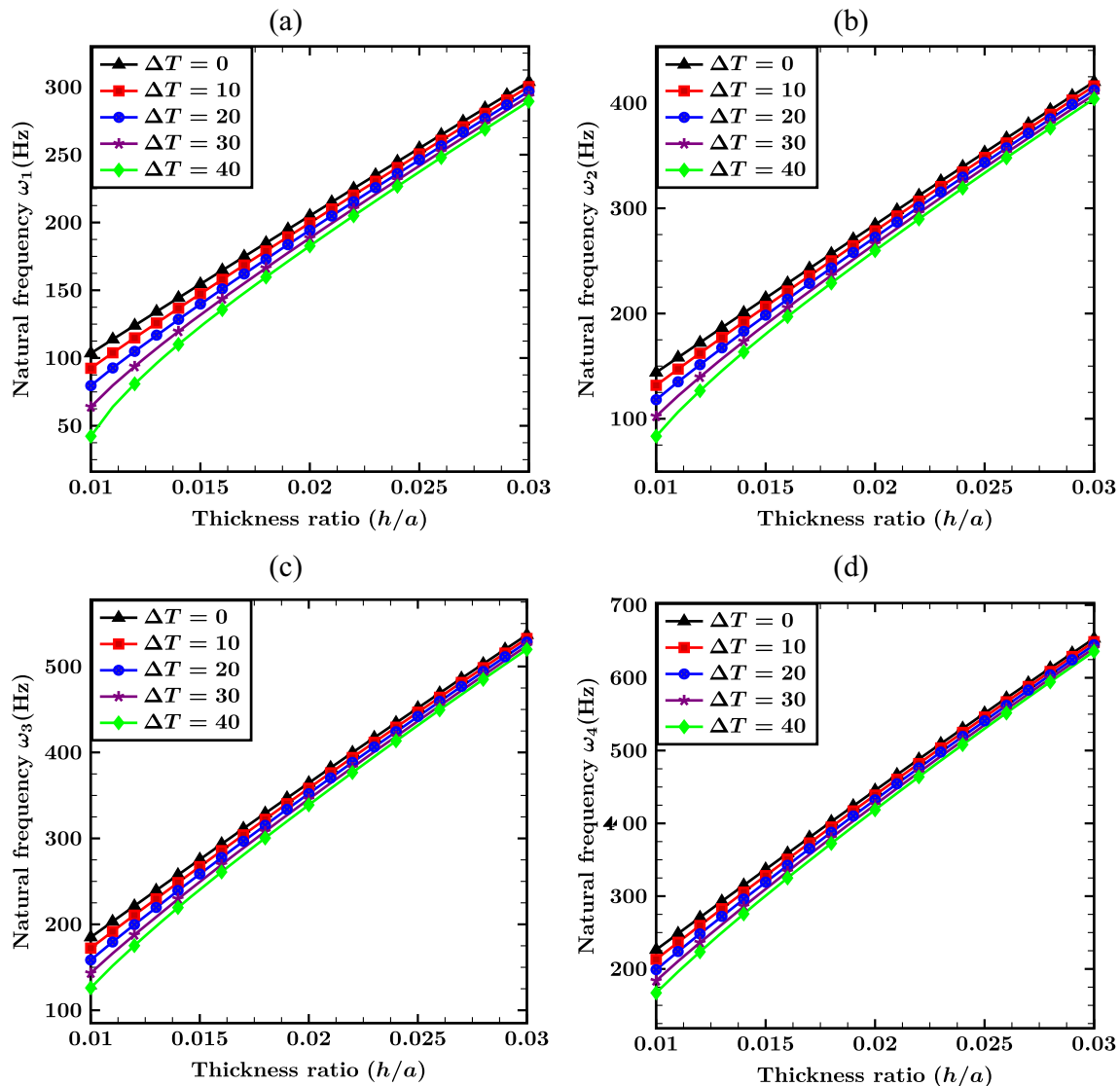


Fig. 11 The first four natural frequencies versus the thickness ratio (h/a) for a nonrotating FG-GRC-ESA plate with boundary conditions C-C-C-C, porosity Type-I and graphene platelets Type-A; ($a = 1$ m, $b/a = 0.3$, $\Omega = 0$, $e_0 = 0.5$, $\Lambda_{GPL} = 0.01$); **a** 1st, **b** 2nd, **c** 3rd and **d** 4th natural frequency

Many parameters have shown to have impact on the final results. In the realm of geometry, as the eccentricity shifts further from the center of the plate, the fundamental frequency tends to decrease. Moreover, the oscillating plate with bigger inner radius is stiffer, and thus its natural frequencies rise. In the realm of material properties, the results recorded the highest natural frequencies for graphene distribution Type-A and the lowest ones for Type-B. The rotational speed and temperature exert arguable influences on the natural frequencies. As an example, the rotational speed has significant impact on those FG-GRC plates whose boundary conditions include a free one. Accordingly, by increasing the rotational speed the natural frequencies tend to grow. On the other hand, the rise in temperature reduces the natural frequencies; however, for a structure with free boundaries (except the inner one), the effect of temperature seems to somewhat diminish for higher modes or greater thickness ratios. The presented technique is anticipated to be recognized as a highly applicable approach for solving oscillatory phenomenon of the eccentric sector-plates in the future.

Declarations

Conflict of interest The authors did not receive support from any organization for the submitted work.

Appendix A

The elements of the reduced stiffness matrix are as follows:

$$Q_{11} = Q_{22} = \frac{E(z)}{1 - \nu(z)^2}, Q_{12} = \frac{\nu(z)E(z)}{1 - \nu(z)^2}, Q_{44} = Q_{55} = Q_{66} = \frac{E(z)}{2(1 + \nu(z))} \quad (67)$$

Appendix B

δv :

$$\begin{aligned} & \sum_{p=1}^{N_r} \sum_{q=1}^{N_\theta} \left\{ \left(\frac{H_{12} \tilde{B}_{ipjq}^{r\theta}}{r_{ij}} + \frac{H_{66} \tilde{B}_{ipjq}^{r\theta}}{r_{ij}} + \frac{H_{22} \tilde{A}_{ipjq}^\theta}{r_{ij}^2} + \frac{H_{66} \tilde{A}_{ipjq}^\theta}{r_{ij}^2} \right) u_{pq} + \right. \\ & \left(\frac{H_{22} \tilde{B}_{ipjq}^\theta}{r_{ij}^2} + H_{66} \tilde{B}_{ipjq}^{r_{ij}} + \frac{H_{66} \tilde{A}_{ipjq}^{r_{ij}}}{r_{ij}} + m_1 \Omega^2 \tilde{\delta}_{ipjq} - \frac{H_{66} \tilde{\delta}_{ipjq}}{r_{ij}^2} \right) v_{pq} \\ & + \left(\frac{H_{12}^f \tilde{B}_{ipjq}^{r\theta}}{r_{ij}} + \frac{H_{66}^f \tilde{B}_{ipjq}^{r\theta}}{r_{ij}} + \frac{H_{22}^f \tilde{A}_{ipjq}^\theta}{r_{ij}^2} + \frac{H_{66}^f \tilde{A}_{ipjq}^\theta}{r_{ij}^2} \right) \varphi_{pq}^r + \left(\frac{H_{12}^g \tilde{B}_{ipjq}^{r\theta}}{r_{ij}} + \frac{H_{66}^g \tilde{B}_{ipjq}^{r\theta}}{r_{ij}} + \frac{H_{22}^g \tilde{A}_{ipjq}^\theta}{r_{ij}^2} + \frac{H_{66}^g \tilde{A}_{ipjq}^\theta}{r_{ij}^2} \right) \psi_{pq}^r \\ & + \left(\frac{H_{22}^f \tilde{B}_{ipjq}^\theta}{r_{ij}^2} + \frac{H_{66}^f \tilde{A}_{ipjq}^{r_{ij}}}{r_{ij}} + H_{66}^f \tilde{B}_{ipjq}^{r_{ij}} + m_f \Omega^2 \tilde{\delta}_{ipjq} - \frac{H_{66}^f \tilde{\delta}_{ipjq}}{r_{ij}^2} \right) \varphi_{pq}^\theta \\ & + \left. \left(\frac{H_{22}^g \tilde{B}_{ipjq}^\theta}{r_{ij}^2} + \frac{H_{66}^g \tilde{A}_{ipjq}^{r_{ij}}}{r_{ij}} + H_{66}^g \tilde{B}_{ipjq}^{r_{ij}} + m_g \Omega^2 \tilde{\delta}_{ipjq} - \frac{H_{66}^g \tilde{\delta}_{ipjq}}{r_{ij}^2} \right) \psi_{pq}^\theta \right\} = m_1 \left(\frac{\partial^2 v}{\partial t^2} \right)_{ij} + 2m_1 \Omega \left(\frac{\partial v}{\partial t} \right)_{ij} \\ & - 2m_f \Omega \left(\frac{\partial \varphi^r}{\partial t} \right)_{ij} - 2m_g \Omega \left(\frac{\partial \psi^r}{\partial t} \right)_{ij} + m_f \left(\frac{\partial^2 \varphi^\theta}{\partial t^2} \right)_{ij} + m_g \left(\frac{\partial^2 \psi^\theta}{\partial t^2} \right)_{ij} \quad (68) \end{aligned}$$

δw :

$$\begin{aligned} & \sum_{p=1}^{N_r} \sum_{q=1}^{N_\theta} \left\{ w_{pq} \left(\frac{2N_{r\theta 0} \tilde{B}_{ipjq}^{r\theta}}{r_{ij}} + \frac{H_{44} \tilde{B}_{ipjq}^\theta}{r_{ij}^2} + \frac{N_{\theta\theta 0} \tilde{B}_{ipjq}^\theta}{r_{ij}^2} + H_{55} \tilde{B}_{ipjq}^{r_{ij}} + N_{rr0} \tilde{B}_{ipjq}^{r_{ij}} + \frac{\partial N_{r\theta 0}}{\partial r} \frac{\tilde{A}_{ipjq}^\theta}{r_{ij}} + \frac{\partial N_{\theta\theta 0}}{\partial \theta} \frac{\tilde{A}_{ipjq}^\theta}{r_{ij}^2} + \frac{\partial N_{rr0}}{\partial r} \tilde{A}_{ipjq}^{r_{ij}} \right. \right. \\ & + \frac{\partial N_{r\theta 0}}{\partial \theta} \frac{\tilde{A}_{ipjq}^{r_{ij}}}{r_{ij}} + \frac{H_{55} \tilde{A}_{ipjq}^{r_{ij}}}{r_{ij}} + \frac{N_{rr0} \tilde{A}_{ipjq}^{r_{ij}}}{r_{ij}} \left. \right) + \left(H_{55}^{f'} \tilde{A}_{ipjq}^{r_{ij}} + \frac{H_{55}^{f'} \tilde{\delta}_{ipjq}}{r_{ij}} \right) \varphi_{pq}^r + \left(H_{55}^{g'} \tilde{A}_{ipjq}^{r_{ij}} + \frac{H_{55}^{g'} \tilde{\delta}_{ipjq}}{r_{ij}} \right) \psi_{pq}^r \\ & + \left. \frac{H_{44}^{f'} \tilde{A}_{ipjq}^\theta}{r_{ij}} \varphi_{pq}^\theta + \frac{H_{44}^{g'} \tilde{A}_{ipjq}^\theta}{r_{ij}} \psi_{pq}^\theta \right\} = m_1 \left(\frac{\partial^2 w}{\partial t^2} \right)_{ij} \quad (69) \end{aligned}$$

$\delta \varphi^r$:

$$\begin{aligned} & \sum_{p=1}^{N_r} \sum_{q=1}^{N_\theta} \left\{ \left(\frac{H_{11}^f \tilde{A}_{ipjq}^{r_{ij}}}{r_{ij}} + H_{11}^f \tilde{B}_{ipjq}^{r_{ij}} + \frac{H_{66}^f \tilde{B}_{ipjq}^\theta}{r_{ij}^2} + m_f \Omega^2 \tilde{\delta}_{ipjq} - \frac{H_{22}^f \tilde{\delta}_{ipjq}}{r_{ij}^2} \right) u_{pq} \right. \\ & + \left(\frac{H_{12}^f \tilde{B}_{ipjq}^{r\theta}}{r_{ij}} + \frac{H_{66}^f \tilde{B}_{ipjq}^{r\theta}}{r_{ij}} - \frac{H_{22}^f \tilde{A}_{ipjq}^\theta}{r_{ij}^2} - \frac{H_{66}^f \tilde{A}_{ipjq}^\theta}{r_{ij}^2} \right) v_{pq} \\ & - H_{55}^{f'} \tilde{A}_{ipjq}^{r_{ij}} w_{pq} + \left(\frac{H_{66}^{ff} \tilde{B}_{ipjq}^\theta}{r_{ij}^2} + H_{11}^{ff} \tilde{B}_{ipjq}^{r_{ij}} + \frac{H_{11}^{ff} \tilde{A}_{ipjq}^{r_{ij}}}{r_{ij}} - H_{55}^{f'f} \tilde{\delta}_{ipjq} + m_{ff} \Omega^2 \tilde{\delta}_{ipjq} - \frac{H_{22}^{ff} \tilde{\delta}_{ipjq}}{r_{ij}^2} \right) \varphi_{pq}^r + \\ & \left. \left(\frac{H_{66}^{fg} \tilde{B}_{ipjq}^\theta}{r_{ij}^2} + H_{11}^{fg} \tilde{B}_{ipjq}^{r_{ij}} + \frac{H_{11}^{fg} \tilde{A}_{ipjq}^{r_{ij}}}{r_{ij}} - H_{55}^{f'g} \tilde{\delta}_{ipjq} + m_{fg} \Omega^2 \tilde{\delta}_{ipjq} - \frac{H_{22}^{fg} \tilde{\delta}_{ipjq}}{r_{ij}^2} \right) \psi_{pq}^r \right\} \end{aligned}$$

$$\begin{aligned}
 & + \left(\frac{H_{12}^{ff} \tilde{B}_{ipjq}^{r\theta}}{r_{ij}} + \frac{H_{66}^{ff} \tilde{B}_{ipjq}^{r\theta}}{r_{ij}} - \frac{H_{22}^{ff} \tilde{A}_{ipjq}^{\theta}}{r_{ij}^2} - \frac{H_{66}^{ff} \tilde{A}_{ipjq}^{\theta}}{r_{ij}^2} \right) \varphi_{pq}^{\theta} + \left(\frac{H_{12}^{fg} \tilde{B}_{ipjq}^{r\theta}}{r_{ij}} + \frac{H_{66}^{fg} \tilde{B}_{ipjq}^{r\theta}}{r_{ij}} - \frac{H_{22}^{fg} \tilde{A}_{ipjq}^{\theta}}{r_{ij}^2} - \frac{H_{66}^{fg} \tilde{A}_{ipjq}^{\theta}}{r_{ij}^2} \right) \psi_{pq}^{\theta} \Big\} \\
 & = m_f \left(\frac{\partial^2 u}{\partial t^2} \right)_{ij} + m_{ff} \left(\frac{\partial^2 \varphi^r}{\partial t^2} \right)_{ij} + m_{fg} \left(\frac{\partial^2 \psi^r}{\partial t^2} \right)_{ij} - 2m_f \Omega \left(\frac{\partial v}{\partial t} \right)_{ij} - 2m_{ff} \Omega \left(\frac{\partial \varphi^{\theta}}{\partial t} \right)_{ij} - 2m_{fg} \Omega \left(\frac{\partial \psi^{\theta}}{\partial t} \right)_{ij} \tag{70}
 \end{aligned}$$

$\delta\varphi^{\theta}$:

$$\begin{aligned}
 & \sum_{p=1}^{N_r} \sum_{q=1}^{N_{\theta}} \left\{ \left(\frac{H_{12}^f \tilde{B}_{ipjq}^{r\theta}}{r_{ij}} + \frac{H_{66}^f \tilde{B}_{ipjq}^{r\theta}}{r_{ij}} + \frac{H_{22}^f \tilde{A}_{ipjq}^{\theta}}{r_{ij}^2} + \frac{H_{66}^f \tilde{A}_{ipjq}^{\theta}}{r_{ij}^2} \right) u_{pq} \right. \\
 & + \left(\frac{H_{22}^f \tilde{B}_{ipjq}^{\theta}}{r_{ij}^2} + \frac{H_{66}^f \tilde{A}_{ipjq}^{r_{ij}}}{r_{ij}} + H_{66}^f \tilde{B}_{ipjq}^{r_{ij}} + m_f \Omega^2 \tilde{\delta}_{ipjq} - \frac{H_{66}^f \tilde{\delta}_{ipjq}}{r_{ij}^2} \right) v_{pq} \\
 & - \frac{H_{44}^f \tilde{A}_{ipjq}^{\theta}}{r_{ij}} w_{pq} + \left(\frac{H_{12}^{ff} \tilde{B}_{ipjq}^{r\theta}}{r_{ij}} + \frac{H_{66}^{ff} \tilde{B}_{ipjq}^{r\theta}}{r_{ij}} + \frac{H_{22}^{ff} \tilde{A}_{ipjq}^{\theta}}{r_{ij}^2} + \frac{H_{66}^{ff} \tilde{A}_{ipjq}^{\theta}}{r_{ij}^2} \right) \varphi_{pq}^r \\
 & + \left(\frac{H_{12}^{fg} \tilde{B}_{ipjq}^{r\theta}}{r_{ij}} + \frac{H_{66}^{fg} \tilde{B}_{ipjq}^{r\theta}}{r_{ij}} + \frac{H_{22}^{fg} \tilde{A}_{ipjq}^{\theta}}{r_{ij}^2} + \frac{H_{66}^{fg} \tilde{A}_{ipjq}^{\theta}}{r_{ij}^2} \right) \psi_{pq}^r + \\
 & \left(\frac{H_{22}^{ff} \tilde{B}_{ipjq}^{\theta}}{r_{ij}^2} + H_{66}^{ff} \tilde{B}_{ipjq}^{r_{ij}} + \frac{H_{66}^{ff} \tilde{A}_{ipjq}^{r_{ij}}}{r_{ij}} - H_{44}^{f'f'} \tilde{\delta}_{ipjq} + m_{ff} \Omega^2 \tilde{\delta}_{ipjq} - \frac{H_{66}^{ff} \tilde{\delta}_{ipjq}}{r_{ij}^2} \right) \varphi_{pq}^{\theta} + \\
 & \left. \left(\frac{H_{22}^{fg} \tilde{B}_{ipjq}^{\theta}}{r_{ij}^2} + H_{66}^{fg} \tilde{B}_{ipjq}^{r_{ij}} + \frac{H_{66}^{fg} \tilde{A}_{ipjq}^{r_{ij}}}{r_{ij}} - H_{44}^{f'g'} \tilde{\delta}_{ipjq} + m_{fg} \Omega^2 \tilde{\delta}_{ipjq} - \frac{H_{66}^{fg} \tilde{\delta}_{ipjq}}{r_{ij}^2} \right) \psi_{pq}^{\theta} \right\} \\
 & = m_f \left(\frac{\partial^2 v}{\partial t^2} \right)_{ij} + m_{ff} \left(\frac{\partial^2 \varphi^{\theta}}{\partial t^2} \right)_{ij} + m_{fg} \left(\frac{\partial^2 \psi^{\theta}}{\partial t^2} \right)_{ij} + 2m_f \Omega \left(\frac{\partial u}{\partial t} \right)_{ij} + 2m_{ff} \Omega \left(\frac{\partial \varphi^r}{\partial t} \right)_{ij} + 2m_{fg} \Omega \left(\frac{\partial \psi^r}{\partial t} \right)_{ij} \tag{71}
 \end{aligned}$$

$\delta\psi^r$:

$$\begin{aligned}
 & \sum_{p=1}^{N_r} \sum_{q=1}^{N_{\theta}} \left\{ \left(\frac{H_{11}^g \tilde{A}_{ipjq}^{r_{ij}}}{r_{ij}} + H_{11}^g \tilde{B}_{ipjq}^{r_{ij}} + \frac{H_{66}^g \tilde{B}_{ipjq}^{\theta}}{r_{ij}^2} + m_g \Omega^2 \tilde{\delta}_{ipjq} - \frac{H_{22}^g \tilde{\delta}_{ipjq}}{r_{ij}^2} \right) u_{pq} \right. \\
 & + \left(\frac{H_{12}^g \tilde{B}_{ipjq}^{r\theta}}{r_{ij}} + \frac{H_{66}^g \tilde{B}_{ipjq}^{r\theta}}{r_{ij}} - \frac{H_{22}^g \tilde{A}_{ipjq}^{\theta}}{r_{ij}^2} - \frac{H_{66}^g \tilde{A}_{ipjq}^{\theta}}{r_{ij}^2} \right) v_{pq} + \\
 & \left(\frac{H_{12}^{fg} \tilde{B}_{ipjq}^{r\theta}}{r_{ij}} + \frac{H_{66}^{fg} \tilde{B}_{ipjq}^{r\theta}}{r_{ij}} - \frac{H_{22}^{fg} \tilde{A}_{ipjq}^{\theta}}{r_{ij}^2} - \frac{H_{66}^{fg} \tilde{A}_{ipjq}^{\theta}}{r_{ij}^2} \right) \varphi_{pq}^{\theta} + \left(\frac{H_{12}^{gg} \tilde{B}_{ipjq}^{r\theta}}{r_{ij}} + \frac{H_{66}^{gg} \tilde{B}_{ipjq}^{r\theta}}{r_{ij}} - \frac{H_{22}^{gg} \tilde{A}_{ipjq}^{\theta}}{r_{ij}^2} - \frac{H_{66}^{gg} \tilde{A}_{ipjq}^{\theta}}{r_{ij}^2} \right) \psi_{pq}^{\theta} + \\
 & \left(\frac{H_{66}^{fg} \tilde{B}_{ipjq}^{\theta}}{r_{ij}^2} + H_{11}^f \tilde{B}_{ipjq}^{r_{ij}} + \frac{H_{11}^{fg} \tilde{A}_{ipjq}^{r_{ij}}}{r_{ij}} - H_{55}^{f'g'} \tilde{\delta}_{ipjq} + m_{fg} \Omega^2 \tilde{\delta}_{ipjq} - \frac{H_{22}^{fg} \tilde{\delta}_{ipjq}}{r_{ij}^2} \right) \varphi_{pq}^r + \\
 & \left. \left(\frac{H_{66}^{gg} \tilde{B}_{ipjq}^{\theta}}{r_{ij}^2} + H_{11}^g \tilde{B}_{ipjq}^{r_{ij}} + \frac{H_{11}^{gg} \tilde{A}_{ipjq}^{r_{ij}}}{r_{ij}} - H_{55}^{g'g'} \tilde{\delta}_{ipjq} + m_{gg} \Omega^2 \tilde{\delta}_{ipjq} - \frac{H_{22}^{gg} \tilde{\delta}_{ipjq}}{r_{ij}^2} \right) \psi_{pq}^r \right\} \\
 & = m_g \left(\frac{\partial^2 u}{\partial t^2} \right)_{ij} + m_{fg} \left(\frac{\partial^2 \varphi^r}{\partial t^2} \right)_{ij} + m_{gg} \left(\frac{\partial^2 \psi^r}{\partial t^2} \right)_{ij} - 2m_g \Omega \left(\frac{\partial v}{\partial t} \right)_{ij} - 2m_{fg} \Omega \left(\frac{\partial \varphi^{\theta}}{\partial t} \right)_{ij} - 2m_{gg} \Omega \left(\frac{\partial \psi^{\theta}}{\partial t} \right)_{ij} \tag{72}
 \end{aligned}$$

$\delta\psi^{\theta}$:

$$\begin{aligned}
 & \sum_{p=1}^{N_r} \sum_{q=1}^{N_{\theta}} \left\{ \left(\frac{H_{12}^g \tilde{B}_{ipjq}^{r\theta}}{r_{ij}} + \frac{H_{66}^g \tilde{B}_{ipjq}^{r\theta}}{r_{ij}} + \frac{H_{22}^g \tilde{A}_{ipjq}^{\theta}}{r_{ij}^2} + \frac{H_{66}^g \tilde{A}_{ipjq}^{\theta}}{r_{ij}^2} \right) u_{pq} \right. \\
 & + \left(\frac{\tilde{B}_{ipjq}^{\theta} H_{22}^g}{r_{ij}^2} + \frac{H_{66}^g \tilde{A}_{ipjq}^{r_{ij}}}{r_{ij}} + H_{66}^g \tilde{B}_{ipjq}^{r_{ij}} + \Omega^2 m_g \tilde{\delta}_{ipjq} - \frac{H_{66}^g \tilde{\delta}_{ipjq}}{r_{ij}^2} \right) v_{pq}
 \end{aligned}$$

$$\begin{aligned}
& - \frac{H_{44}^{g'} \tilde{A}_{ipjq}^{\theta}}{r_{ij}} w_{pq} + \left(\frac{H_{12}^{fg} \tilde{B}_{ipjq}^{r\theta}}{r_{ij}} + \frac{H_{66}^{fg} \tilde{B}_{ipjq}^{r\theta}}{r_{ij}} + \frac{H_{22}^{fg} \tilde{A}_{ipjq}^{\theta}}{r_{ij}^2} + \frac{H_{66}^{fg} \tilde{A}_{ipjq}^{\theta}}{r_{ij}^2} \right) \phi_{pq}^r + \\
& \left(\frac{H_{12}^{gg} \tilde{B}_{ipjq}^{r\theta}}{r_{ij}} + \frac{H_{66}^{gg} \tilde{B}_{ipjq}^{r\theta}}{r_{ij}} + \frac{H_{22}^{gg} \tilde{A}_{ipjq}^{\theta}}{r_{ij}^2} + \frac{H_{66}^{gg} \tilde{A}_{ipjq}^{\theta}}{r_{ij}^2} \right) \psi_{pq}^r + \\
& \left(\frac{H_{22}^{fg} \tilde{B}_{ipjq}^{\theta}}{r_{ij}^2} + H_{66}^{fg} \tilde{B}_{ipjq}^{r_{ij}} + \frac{H_{66}^{fg} \tilde{A}_{ipjq}^{r_{ij}}}{r_{ij}} - H_{44}^{f'g'} \tilde{\delta}_{ipjq} + m_{fg} \Omega^2 \tilde{\delta}_{ipjq} - \frac{H_{66}^{fg} \tilde{\delta}_{ipjq}}{r_{ij}^2} \right) \phi_{pq}^{\theta} + \\
& \left. \left(\frac{H_{22}^{gg} \tilde{B}_{ipjq}^{\theta}}{r_{ij}^2} + H_{66}^{gg} \tilde{B}_{ipjq}^{r_{ij}} + \frac{H_{66}^{gg} \tilde{A}_{ipjq}^{r_{ij}}}{r_{ij}} - H_{44}^{g'g'} \tilde{\delta}_{ipjq} + m_{gg} \Omega^2 \tilde{\delta}_{ipjq} - \frac{H_{66}^{gg} \tilde{\delta}_{ipjq}}{r_{ij}^2} \right) \psi_{pq}^{\theta} \right\} \\
& = m_g \left(\frac{\partial^2 v}{\partial t^2} \right)_{ij} + m_{fg} \left(\frac{\partial^2 \phi^{\theta}}{\partial t^2} \right)_{ij} + m_{gg} \left(\frac{\partial^2 \psi^{\theta}}{\partial t^2} \right)_{ij} + 2m_g \Omega \left(\frac{\partial u}{\partial t} \right)_{ij} + 2m_{fg} \Omega \left(\frac{\partial \phi^r}{\partial t} \right)_{ij} + 2m_{gg} \Omega \left(\frac{\partial \psi^r}{\partial t} \right)_{ij}
\end{aligned} \tag{73}$$

References

1. Gojny, F.H., Wichmann, M.H.G., Köpke, U., et al.: Carbon nanotube-reinforced epoxy-composites: enhanced stiffness and fracture toughness at low nanotube content. *Compos. Sci. Technol.* **64**, 2363–2371 (2004)
2. Rafiee, M.A., Rafiee, J., Wang, Z., et al.: Enhanced mechanical properties of nanocomposites at low graphene content. *ACS Nano* **3**, 3884–3890 (2009)
3. García-Macías, E., Rodríguez-Tembleque, L., Sáez, A.: Bending and free vibration analysis of functionally graded graphene vs. carbon nanotube reinforced composite plates. *Compos. Struct.* **186**, 123–138 (2018). <https://doi.org/10.1016/j.compstruct.2017.11.076>
4. Karimiasl, M., Ebrahimi, F., Mahesh, V.: On nonlinear vibration of sandwiched polymer- CNT/GPL-fiber nanocomposite nanoshells. *Thin-Walled Struct.* **146**, 106431 (2020). <https://doi.org/10.1016/j.tws.2019.106431>
5. Feng, C., Kitipornchai, S., Yang, J.: Nonlinear free vibration of functionally graded polymer composite beams reinforced with graphene nanoplatelets (GPLs). *Eng. Struct.* **140**, 110–119 (2017)
6. Feng, C., Kitipornchai, S., Yang, J.: Nonlinear bending of polymer nanocomposite beams reinforced with non-uniformly distributed graphene platelets (GPLs). *Compos. Part B Eng.* **110**, 132–140 (2017)
7. Kitipornchai, S., Chen, D., Yang, J.: Free vibration and elastic buckling of functionally graded porous beams reinforced by graphene platelets. *Mater. Des.* **116**, 656–665 (2017)
8. Bidzard, A., Malekzadeh, P., Mohebpour, S.R.: Vibration of multilayer FG-GPLRC toroidal panels with elastically restrained against rotation edges. *Thin-Walled Struct.* **143**, 106209 (2019). <https://doi.org/10.1016/j.tws.2019.106209>
9. Ansari, R., Torabi, J., Hasrati, E.: Postbuckling analysis of axially-loaded functionally graded GPL-reinforced composite conical shells. *Thin-Walled Struct.* **148**, 106594 (2020). <https://doi.org/10.1016/j.tws.2019.106594>
10. Duarte, I., Ventura, E., Olhero, S., Ferreira, J.M.F.: An effective approach to reinforced closed-cell Al-alloy foams with multiwalled carbon nanotubes. *Carbon* **95**, 589–600 (2015)
11. Rashad, M., Pan, F., Tang, A., Asif, M.: Effect of graphene nanoplatelets addition on mechanical properties of pure aluminum using a semi-powder method. *Prog. Nat. Sci. Mater. Int.* **24**, 101–108 (2014)
12. Bartolucci, S.F., Paras, J., Rafiee, M.A., et al.: Graphene–aluminum nanocomposites. *Mater. Sci. Eng. A* **528**, 7933–7937 (2011)
13. Duarte, I., Ventura, E., Olhero, S., Ferreira, J.M.F.: A novel approach to prepare aluminium-alloy foams reinforced by carbon-nanotubes. *Mater. Lett.* **160**, 162–166 (2015)
14. Mirjavadi, S.S., Matin, A., Shafiei, N., et al.: Thermal buckling behavior of two-dimensional imperfect functionally graded microscale-tapered porous beam. *J. Therm. Stress* **40**, 1201–1214 (2017). <https://doi.org/10.1080/01495739.2017.1332962>
15. Amir, S., Arshid, E., Rasti-Alhosseini, S.M.A., Loghman, A.: Quasi-3D tangential shear deformation theory for size-dependent free vibration analysis of three-layered FG porous micro rectangular plate integrated by nano-composite faces in hygrothermal environment. *J. Therm. Stress* **43**, 133–156 (2020). <https://doi.org/10.1080/01495739.2019.1660601>
16. Ghadiri, M., SafarPour, H.: Free vibration analysis of size-dependent functionally graded porous cylindrical microshells in thermal environment. *J. Therm. Stress* **40**, 55–71 (2017). <https://doi.org/10.1080/01495739.2016.1229145>
17. Ahmadi, H., Foroutan, K.: Nonlinear static and dynamic thermal buckling analysis of imperfect multilayer FG cylindrical shells with an FG porous core resting on nonlinear elastic foundation. *J. Therm. Stress* **43**, 629–649 (2020). <https://doi.org/10.1080/01495739.2020.1727802>
18. Chen, D., Yang, J., Kitipornchai, S.: Nonlinear vibration and postbuckling of functionally graded graphene reinforced porous nanocomposite beams. *Compos. Sci. Technol.* **142**, 235–245 (2017). <https://doi.org/10.1016/j.compscitech.2017.02.008>
19. Barati, M.R., Zenkour, A.M.: Post-buckling analysis of refined shear deformable graphene platelet reinforced beams with porosities and geometrical imperfection. *Compos. Struct.* **181**, 194–202 (2017)
20. Li, Z., Zheng, J.: Structural failure performance of the encased functionally graded porous cylinder consolidated by graphene platelet under uniform radial loading. *Thin-Walled Struct.* **146**, 106454 (2020). <https://doi.org/10.1016/j.tws.2019.106454>

21. Panah, M., Khorshidvand, A.R., Khorsandijou, S.M., Jabbari, M.: Pore pressure and porosity effects on bending and thermal postbuckling behavior of FG saturated porous circular plates. *J. Therm. Stress* **42**, 1083–1109 (2019). <https://doi.org/10.1080/01495739.2019.1614502>
22. Žur, K.K.: Free vibration analysis of elastically supported functionally graded annular plates via quasi-Green's function method. *Compos. Part B Eng.* **144**, 37–55 (2018). <https://doi.org/10.1016/j.compositesb.2018.02.019>
23. Allahkarami, F.: Dynamic buckling of functionally graded multilayer graphene nanocomposite annular plate under different boundary conditions in thermal environment. *Eng. Comput.* **38**, 583–606 (2020)
24. Hosseini-Hashemi, S., Derakhshani, M., Fadaee, M.: An accurate mathematical study on the free vibration of stepped thickness circular/annular Mindlin functionally graded plates. *Appl. Math. Model.* **37**, 4147–4164 (2013)
25. Shariyat, M., Alipour, M.M.: A power series solution for vibration and complex modal stress analyses of variable thickness viscoelastic two-directional FGM circular plates on elastic foundations. *Appl. Math. Model.* **37**, 3063–3076 (2013)
26. Shahrestani, M.G., Azhari, M., Foroughi, H.: Elastic and inelastic buckling of square and skew FGM plates with cutout resting on elastic foundation using isoparametric spline finite strip method. *Acta Mech.* **229**, 2079–2096 (2018). <https://doi.org/10.1007/s00707-017-2082-2>
27. Shaterzadeh, A., Behzad, H., Shariyat, M.: Stability analysis of composite perforated annular sector plates under thermomechanical loading by finite element method. *Int. J. Struct. Stab. Dyn.* **18**, 1850100 (2018)
28. Hasheminejad, S.M., Vaezian, S.: Free vibration analysis of an elliptical plate with eccentric elliptical cut-outs. *Meccanica* **49**, 37–50 (2014)
29. Cheng, L., Li, Y.Y., Yam, L.H.: Vibration analysis of annular-like plates. *J. Sound Vib.* **262**, 1153–1170 (2003)
30. Hasheminejad, S.M., Ghaheer, A., Vaezian, S.: Exact solution for free in-plane vibration analysis of an eccentric elliptical plate. *Acta Mech.* **224**, 1609–1624 (2013). <https://doi.org/10.1007/s00707-013-0829-y>
31. Fadaee, M., Ilkhani, M.R.: Study on the effect of an eccentric hole on the vibrational behavior of a graphene sheet using an analytical approach. *Acta Mech.* **226**, 1395–1407 (2015). <https://doi.org/10.1007/s00707-014-1259-1>
32. Askari, E., Jeong, K.-H., Amabili, M.: A novel mathematical method to analyze the free vibration of eccentric annular plates. *J. Sound Vib.* **484**, 115513 (2020). <https://doi.org/10.1016/j.jsv.2020.115513>
33. Askari, E., Jeong, K.-H., Ahn, K.-H., Amabili, M.: A mathematical approach to study fluid-coupled vibration of eccentric annular plates. *J. Fluids Struct.* **98**, 103129 (2020). <https://doi.org/10.1016/j.jfluidstructs.2020.103129>
34. Malekzadeh, P., Setoodeh, A.R., Shojae, M.: Vibration of FG-GPLs eccentric annular plates embedded in piezoelectric layers using a transformed differential quadrature method. *Comput. Methods Appl. Mech. Eng.* **340**, 451–479 (2018)
35. Arafat, H.N., Nayfeh, A.H., Faris, W.: Natural frequencies of heated annular and circular plates. *Int. J. Solids Struct.* **41**, 3031–3051 (2004)
36. Mousavi, S.M.J., Sharifi, P., Fattahi, I., Mohammadi, H.: On the tuning of static pull-in instability and nonlinear vibrations of functionally graded micro-resonators with three different configurations. *J. Braz. Soc. Mech. Sci. Eng.* **42**, 339 (2020). <https://doi.org/10.1007/s40430-020-02426-y>
37. Salighe, S., Mohammadi, H.: Semi-active nonlinear vibration control of a functionally graded material rotating beam with uncertainties, using a frequency estimator. *Compos. Struct.* (2019). <https://doi.org/10.1016/j.compstruct.2018.11.060>
38. Malekzadeh, P., Shahpari, S.A., Ziaee, H.R.: Three-dimensional free vibration of thick functionally graded annular plates in thermal environment. *J. Sound Vib.* **329**, 425–442 (2010)
39. Lal, R., Saini, R.: Vibration analysis of functionally graded circular plates of variable thickness under thermal environment by generalized differential quadrature method. *J. Vib. Control* **26**, 73–87 (2020)
40. Zhao, T., Li, K., Ma, H.: Study on dynamic characteristics of a rotating cylindrical shell with uncertain parameters. *Anal. Math. Phys.* **12**, 1–28 (2022)
41. Zhao, T.Y., Jiang, L.P., Pan, H.G., et al.: Coupled free vibration of a functionally graded pre-twisted blade-shaft system reinforced with graphene nanoplatelets. *Compos. Struct.* **262**, 113362 (2021)
42. Zhao, T.Y., Cui, Y.S., Pan, H.G., et al.: Free vibration analysis of a functionally graded graphene nanoplatelet reinforced disk-shaft assembly with whirl motion. *Int. J. Mech. Sci.* **197**, 106335 (2021)
43. Zhao, T.Y., Ma, Y., Zhang, H.Y., et al.: Free vibration analysis of a rotating graphene nanoplatelet reinforced pre-twist blade-disk assembly with a setting angle. *Appl. Math. Model.* **93**, 578–596 (2021)
44. Zhao, T.Y., Yan, K., Li, H.W., Wang, X.: Study on theoretical modeling and vibration performance of an assembled cylindrical shell-plate structure with whirl motion. *Appl. Math. Model.* **110**, 618–632 (2022)
45. Hu, Y.D., Wang, T.: Nonlinear free vibration of a rotating circular plate under the static load in magnetic field. *Nonlinear Dyn.* **85**, 1825–1835 (2016)
46. Chen, Y.-R., Chen, L.-W.: Vibration and stability of rotating polar orthotropic sandwich annular plates with a viscoelastic core layer. *Compos. Struct.* **78**, 45–57 (2007)
47. Bashmal, S., Bhat, R., Rakheja, S.: In-plane free vibration of circular annular disks. *J. Sound Vib.* **322**, 216–226 (2009)
48. Maretic, R.: Transverse vibration and stability of an eccentric rotating circular plate. *J. Sound Vib.* **280**, 467–478 (2005)
49. Bagheri, E., Jahangiri, M.: Analysis of in-plane vibration and critical speeds of the functionally graded rotating disks. *Int. J. Appl. Mech.* **11**, 1950020 (2019)
50. Yang, Y.B., Kang, J.H.: Vibration and buckling analysis of a rotating annular plate subjected to a compressive centrifugal body force. *Int. J. Struct. Stab. Dyn.* **18**, 1850097 (2018)
51. Younesian, D., Aleghafourian, M.H., Esmailzadeh, E.: Vibration analysis of circular annular plates subjected to peripheral rotating transverse loads. *J. Vib. Control* **21**, 1443–1455 (2015)
52. Setoodeh, A.R., Shojae, M., Malekzadeh, P.: Application of transformed differential quadrature to free vibration analysis of FG-CNTRC quadrilateral spherical panel with piezoelectric layers. *Comput. Methods Appl. Mech. Eng.* **335**, 510–537 (2018)
53. Shojae, M., Setoodeh, A.R., Malekzadeh, P.: Vibration of functionally graded CNTs-reinforced skewed cylindrical panels using a transformed differential quadrature method. *Acta Mech.* **228**, 2691–2711 (2017)
54. Setoodeh, A.R., Shojae, M.: Application of TW-DQ method to nonlinear free vibration analysis of FG carbon nanotube-reinforced composite quadrilateral plates. *Thin-Walled Struct.* **108**, 1–11 (2016)

55. Li, Q., Wu, D., Chen, X., et al.: Nonlinear vibration and dynamic buckling analyses of sandwich functionally graded porous plate with graphene platelet reinforcement resting on Winkler-Pasternak elastic foundation. *Int. J. Mech. Sci.* **148**, 596–610 (2018). <https://doi.org/10.1016/j.ijmecsci.2018.09.020>
56. Safarpour, H., Hajilak, Z.E., Habibi, M.: A size-dependent exact theory for thermal buckling, free and forced vibration analysis of temperature dependent FG multilayer GPLRC composite nanostructures resting on elastic foundation. *Int. J. Mech. Mater. Des.* **15**, 569–583 (2019)
57. Fazelzadeh, S.A., Rahmani, S., Ghavanloo, E., Marzocca, P.: Thermoelastic vibration of doubly-curved nano-composite shells reinforced by graphene nanoplatelets. *J. Therm. Stress* **42**, 1–17 (2019)
58. An, D., Bz, T., Polit, O., et al.: Large amplitude free flexural vibrations of functionally graded graphene platelets reinforced porous composite curved beams using finite element based on trigonometric shear deformation theory. *Int. J. Non Linear Mech.* **116**, 302–317 (2019). <https://doi.org/10.1016/j.ijnonlinmec.2019.07.010>
59. Reddy, J.N.: *Theory and Analysis of Elastic Plates and Shells*. CRC Press (2006)
60. Dym, C.L., Shames, I.H.: *Solid Mechanics: A Variational Approach*, Augmented Springer, New York (2013)
61. Setoodeh, A.R., Shojaee, M., Malekzadeh, P.: Vibrational behavior of doubly curved smart sandwich shells with FG-CNTRC face sheets and FG porous core. *Compos. Part B Eng.* **165**, 798–822 (2019). <https://doi.org/10.1016/j.compositesb.2019.01.022>
62. Hong, C.-C.: Thermal vibration of thick FGM spherical shells by using TSDT. *Int. J. Mech. Mater. Des.* **17**, 367–380 (2021)
63. Mehri, M., Asadi, H., Wang, Q.: Buckling and vibration analysis of a pressurized CNT reinforced functionally graded truncated conical shell under an axial compression using HDQ method. *Comput. Methods Appl. Mech. Eng.* **303**, 75–100 (2016). <https://doi.org/10.1016/j.cma.2016.01.017>
64. Yas, M.H., Rahimi, S.: Thermal vibration of functionally graded porous nanocomposite beams reinforced by graphene platelets. *Appl. Math. Mech.* **41**, 1209–1226 (2020). <https://doi.org/10.1007/s10483-020-2634-6>
65. Nagaya, K.: Vibration of a viscoelastic plate having a circular outer boundary and an eccentric circular inner boundary for various edge conditions. *J. Sound Vib.* **63**, 73–85 (1979)

Publisher's Note Springer Nature remains neutral with regard to jurisdictional claims in published maps and institutional affiliations.

Springer Nature or its licensor (e.g. a society or other partner) holds exclusive rights to this article under a publishing agreement with the author(s) or other rightsholder(s); author self-archiving of the accepted manuscript version of this article is solely governed by the terms of such publishing agreement and applicable law.